Stellar mass as a galaxy cluster mass proxy: application to the Dark Energy Survey redMaPPer clusters

Monthly Notices
of the
ROYAL ASTRONOMICAL SOCIETY

MNRAS **493,** 4591–4606 (2020)
Advance Access publication 2020 February 21

doi:10.1093/mnras/staa526

Stellar mass as a galaxy cluster mass proxy: application to the Dark Energy Survey redMaPPer clusters

A. Palmese ,[1,2]★ J. Annis,[1] J. Burgad,[3] A. Farahi,[4] M. Soares-Santos,[5] B. Welch,[6] M. da Silva Pereira,[5] H. Lin,[1] S. Bhargava,[7] D. L. Hollowood,[8] R. Wilkinson,[7] P. Giles,[7] T. Jeltema,[8] A. K. Romer,[7] A. E. Evrard,[9,10] M. Hilton,[11] C. Vergara Cervantes,[7] A. Bermeo,[7] J. Mayers,[7] J. DeRose,[12,13] D. Gruen,[12,13,14] W. G. Hartley,[2,15] O. Lahav,[2] B. Leistedt,[16] T. McClintock,[17] E. Rozo,[17] E. S. Rykoff,[13,14] T. N. Varga,[18,19] R. H. Wechsler,[12,13,14] Y. Zhang,[1] S. Avila,[20] D. Brooks,[2] E. Buckley-Geer,[1] D. L. Burke,[13,14] A. Carnero Rosell,[21,22] M. Carrasco Kind,[23,24] J. Carretero,[25] F. J. Castander,[26,27] C. Collins,[28] L. N. da Costa,[22,29] S. Desai,[30] J. De Vicente,[21] H. T. Diehl,[1] J. P. Dietrich,[31,32] P. Doel,[2] B. Flaugher,[1] P. Fosalba,[26,27] J. Frieman,[1,6] J. García-Bellido,[33] D. W. Gerdes,[9,10] R. A. Gruendl,[23,24] J. Gschwend,[22,29] G. Gutierrez,[1] K. Honscheid,[34,35] D. J. James,[36] E. Krause,[37] K. Kuehn,[38] N. Kuropatkin,[1] A. Liddle,[39] M. Lima,[22,40] M. A. G. Maia,[22,29] R. G. Mann,[41] J. L. Marshall,[42,43] F. Menanteau,[23,24] R. Miquel,[25,44] R. L. C. Ogando,[22,29] A. A. Plazas,[45] A. Roodman,[13,14] P. Rooney,[7] M. Sahlen,[46] E. Sanchez,[21] V. Scarpine,[1] M. Schubnell,[10] S. Serrano,[26,27] I. Sevilla-Noarbe,[21] F. Sobreira,[22,47] J. Stott,[48,49] E. Suchyta,[50] M. E. C. Swanson,[24] G. Tarle,[10] D. Thomas,[20] D. L. Tucker,[1] P. T. P. Viana,[51,52] V. Vikram,[53] and A. R. Walker[54] (DES Collaboration)

Affiliations are listed at the end of the paper

Accepted 2020 February 17. Received 2020 February 12; in original form 2019 March 20

ABSTRACT

We introduce a galaxy cluster mass observable, $\mu_\star$, based on the stellar masses of cluster members, and we present results for the Dark Energy Survey (DES) Year 1 (Y1) observations. Stellar masses are computed using a Bayesian model averaging method, and are validated for DES data using simulations and COSMOS data. We show that $\mu_\star$ works as a promising mass proxy by comparing our predictions to X-ray measurements. We measure the X-ray temperature–$\mu_\star$ relation for a total of 129 clusters matched between the wide-field DES Y1 redMaPPer catalogue and *Chandra* and *XMM* archival observations, spanning the redshift range $0.1 < z < 0.7$. For a scaling relation that is linear in logarithmic space, we find a slope of $\alpha = 0.488 \pm 0.043$ and a scatter in the X-ray temperature at fixed $\mu_\star$ of $\sigma_{\ln T_X|\mu_\star} = 0.266^{+0.019}_{-0.020}$ for the joint sample. By using the halo mass scaling relations of the X-ray temperature from the Weighing the Giants program, we further derive the $\mu_\star$-conditioned scatter in mass, finding $\sigma_{\ln M|\mu_\star} = 0.26^{+0.15}_{-0.10}$. These results are competitive with well-established cluster mass proxies used for cosmological analyses, showing that $\mu_\star$ can be used as a reliable and physically motivated mass proxy to derive cosmological constraints.

Key words: surveys – galaxies: clusters: general – galaxies: evolution – galaxies: haloes – cosmology: observations.

★ E-mail: palmese@fnal.gov

1 INTRODUCTION

Galaxy clusters are fundamental cosmological probes for large galaxy surveys such as the Dark Energy Survey (DES; The Dark Energy Survey Collaboration 2005). The estimation of the cosmological parameters from clusters abundance is allowed by the dependence of the dark matter halo mass function on cosmology (Press & Schechter 1974; Sheth & Tormen 2002; Tinker et al. 2008), but it requires estimates of cluster total masses from the observables of our galaxy survey. In practice, we seek cluster mass observables (or mass proxies) that tightly correlate with the total cluster mass. In other words, they exhibit a low scatter in total mass at fixed mass proxy (and vice versa).

Several cluster finders are based on the cluster red sequence (e.g. Koester et al. 2007; Hao et al. 2010; Oguri 2014; Rykoff et al. 2014). Amongst those, redMaPPer (Rykoff et al. 2014) has been extensively studied and its mass proxy, the richness λ, calibrated for large photometric surveys such as the Sloan Digital Sky Survey (SDSS) and the DES over the past decade (Rozo et al. 2009a, b, 2011; Melchior et al. 2016; Rykoff et al. 2016; Simet et al. 2017; Costanzi et al. 2019). On the other hand, there exists broad evidence that the content of clusters includes a non-negligible fraction of bluer, star-forming galaxies that do not follow the red-sequence colour–magnitude relation, in particular towards increasing redshift (Oemler 1974; Butcher & Oemler 1978; Butcher & Oemler 1984; Donahue et al. 2002; Zhang et al. 2017). This effect is known as the Butcher–Oemler effect. Whether the inclusion of the blue cloud can improve cluster mass estimates for cosmology is a matter of debate (e.g. Rozo et al. 2011) and depends on the survey characteristics. At higher redshifts, the blue fraction becomes more significant (though the number count of blue galaxies over all members can also reach $\sim$ 30 per cent below redshift $\sim$0.3; Zu & Mandelbaum 2016) and the red sequence is not as distinguishable in colour–magnitude space as at lower redshift. In these regimes, the inclusion of the bluer members may play a significant role in cluster abundance studies of DES and other ongoing and future photometric surveys (the Large Synoptic Sky Telescope, LSST, Ivezić et al. 2008; Euclid, Laureijs et al. 2011) that push towards higher redshifts, $z = 1$ and beyond.

One clear advantage of including blue galaxies in cluster catalogues is in studying cluster properties and their evolution with redshift, in particular the Butcher–Oemler effect and quenching mechanisms. Moreover, cluster finders able to identify also cluster members that do not belong to the red sequence (Miller et al. 2005; Soares-Santos et al. 2011) already exist. For these reasons, we develop a low scatter mass proxy for cluster finders that is not red sequence based.

Previous works (e.g. Andreon 2012) have exploited stellar masses as a possible cluster mass proxy. We here extend those studies by using a larger sample of X-ray clusters for calibration and by complementing the stellar mass estimates with a membership probability scheme presented in a companion paper, Welch et al. (in preparation). A feasibility study for stellar mass computation with DES data has already been carried out in Palmese et al. (2016), where they found that stellar masses of cluster members can be recovered within 25 per cent of *Hubble Space Telescope* Cluster Lensing and Supernovae Survey with Hubble (CLASH) values. The use of the stellar mass content as a probe of total cluster mass is empirically but also physically motivated by the stellar-to-halo connection (see e.g. Wechsler & Tinker 2018 for a review), which follows a linear relation in the logarithm of masses at cluster scales. An analysis of the scaling relation for the stellar content with halo mass thus has interesting implications not only for cosmological analysis, but also for the stellar-to-halo mass relation (SHMR), which is of interest to understand galaxy evolution within clusters (see Palmese et al., in preparation for implications on the SHMR from the whole DES redMaPPer sample). In fact, the SHMR can be expressed as a joint likelihood of mass and observable properties. Because of this, the stellar mass can potentially be more tightly related to the total mass of clusters on the individual halo basis, than galaxy number counts would. On the other hand, projection effects due to foreground and background galaxies being confused with cluster members, are perhaps one of the most problematic issue in cluster cosmology with richness (Costanzi et al. 2019). These effects are likely to affect our stellar mass observable in a similar way to λ, because of the similarities between the two methods. However, these effects could be alleviated by the fact that the very massive central galaxies tend to dominate the total mass, making our mass proxy less sensitive to field galaxies contamination (as recently shown in Bradshaw et al. 2020).

We therefore apply our method to a well-established cluster catalogue, the DES Year 1 (Y1) redMaPPer catalogue, matched to X-ray observations. Nevertheless, this mass proxy can easily be used with other, non-red-sequence based, cluster finders. We also test our cluster stellar mass estimates against simulations.

The X-ray temperature and luminosity of clusters represent a well-known, low scatter mass proxy for cluster mass, for which total mass scaling relations have been studied in depth (e.g. Mantz et al. 2016). The formalism by Evrard et al. (2014) allows us to link the scaling relations of different mass proxies when a lognormal covariance is assumed around the mean scaling relations of the mass proxies. It is thus possible to derive an estimate of the scatter on the total mass of clusters by using the scaling relations between our mass proxy and the X-ray temperature, and between the X-ray temperature and the total mass of clusters. Such estimates provide essential prior information for our mass proxy–mass scatter in a cosmological analysis with cluster abundance.

In this work, we present a stellar mass-based cluster mass proxy, called $\mu_\star$, and assess its performance as a mass proxy using archival X-ray data. This paper is divided into five sections. In Section 2, we describe the DES galaxy catalogue, the Y1 redMaPPer catalogue, and the X-ray cluster catalogues used. In Section 3, we present a new method to compute galaxy stellar masses that uses a Bayesian model averaging (BMA) technique. We then introduce the scheme to produce our stellar mass proxy $\mu_\star$ and briefly describe the membership probability assignment. We also present the method used to compute the X-ray scaling relations and the mass scatter. Section 4 contains measurements of the $T_{\rm X}$–$\mu_\star$ relation and scatter constraints, both for the temperature scatter and the total cluster mass scatter. Section 5 contains discussion and conclusions.

Throughout this work, we assume a ΛCDM flat cosmology with $H_0 = 70\,{\rm km\,s^{-1}\,Mpc^{-1}}$, $\Omega_{\rm m} = 0.3$, $\Omega_\Lambda = 0.7$. The notation adopted for the cluster mass and radius follows the one often used in the literature. The radii of spheres around the cluster centre are written as $r_{\Delta{\rm m}}$ and $r_{\Delta{\rm c}}$ where Δ is the overdensity of the sphere with respect to the mean matter density (subscript m) or the critical density (subscript c) at the cluster redshift. Masses inside those spheres are therefore $M_{\Delta{\rm m}} = \Delta \frac{4\pi}{3} r^3_{\Delta{\rm m}} \rho_{\rm m}$ and similarly for $M_{\Delta{\rm c}}$. In the following, we quote $\Delta = 200$, which roughly corresponds to the density contrast at virialization for a dark matter halo at $z = 0$. Logarithms indicated as ln are in base e, and Log are in base 10. Errors are 68 per cent confidence level unless otherwise stated.

2 DATA

2.1 DES Year 1 data

The DES[1] is an optical-to-near-infrared survey that imaged 5000 deg^2 of the South Galactic Cap in the *grizY* bands over 575 nights spanning almost 6 yr. The survey was carried out using a ∼3 deg^2 CCD camera (the DECam, see Flaugher et al. 2015) mounted on the Blanco 4-m telescope at the Cerro Tololo Inter-American Observatory (CTIO) in Chile. DES started in 2012 with a testing period (2012 November–2013 February) called DES Science Verification (SV).[2] The data used here come from the first year of observations (2013 September–2014 February, Diehl et al. 2014) and cover 1839 deg^2 with up to four passes per filter. The data are available at http://des.ncsa.illinois.edu/releases/y1a1.

The survey strategy is designed to optimize the photometric calibration by tiling each region of the survey with several overlapping pointings in each band. This provides uniformity of coverage and control of systematic photometric errors. This strategy allows DES to determine photometric redshifts of ∼300 million galaxies to an accuracy of $\sigma(z) \simeq 0.07$ out to $z \gtrsim 1$, with some dependence on redshift and galaxy type, and cluster photometric redshifts to $\sigma(z) \sim 0.02$ or better out to $z \simeq 1.3$ (The Dark Energy Survey Collaboration 2005). It has already found ∼400 million objects, including stars and galaxies, from the first three years of operations (Abbott et al. 2018), and ∼ 80 000 galaxy clusters from the first year.

The DES Data Management (DESDM) pipeline was used for data reduction, as described in detail in Sevilla et al. (2011), Desai et al. (2012), and Mohr et al. (2012). The process includes calibration of the single-epoch images, which are co-added after background subtraction and then cut into tiles. The source catalogue was created using SOURCE EXTRACTOR (SEXTRACTOR, Bertin & Arnouts 1996) to detect objects on the *riz* co-added images. The median 10σ limiting magnitudes of Y1 data for galaxies are $g = 23.4$, $r = 23.2$, $i = 22.5$, $z = 21.8$, and $Y = 20.1$. Drlica-Wagner et al. (2018) made further selections to produce a high-quality object catalogue called the Y1A1 'gold' catalogue.

The cluster catalogue used here is the cosmology Y1 redMaPPer catalogue v6.4.14 with richness $\lambda > 5$, which consists of 87 297 clusters. This sample is then matched to archival X-ray observations from *Chandra* and X-ray MultiMirror Mission (*XMM*). We use these X-ray data to measure an X-ray temperature at the position of redMaPPer clusters, rather than cross-matching with existing X-ray cluster catalogues. The 2D distribution of richness and redshift of the matched samples is shown in Fig. 1. The centre position (given by the galaxy with the highest central probability $p_{\rm cen}$) and the cluster redshift are the only outputs used from this catalogue. The galaxies associated with each cluster are taken from the Y1A1 gold catalogue. We select objects with MODEST_CLASS = 1 in order to exclude sources that are likely not to be galaxies.

While the cluster catalogue is based on Y1 data, the photometry comes from the deeper Year 3 data (median 10σ co-added catalogue depths for a 1.95 arcsec diameter aperture: $g = 24.33$, $r = 24.08$, $i = 23.44$, $z = 22.69$, and $Y = 21.44$ mag; Abbott et al. 2018). The photometry is the result of the Multi-Object Fitting (MOF) pipeline that uses the NGMIX code.[3]

In order to compute the membership probabilities (as described in Section 3.2), we use photometric redshifts (photo-z's) from the

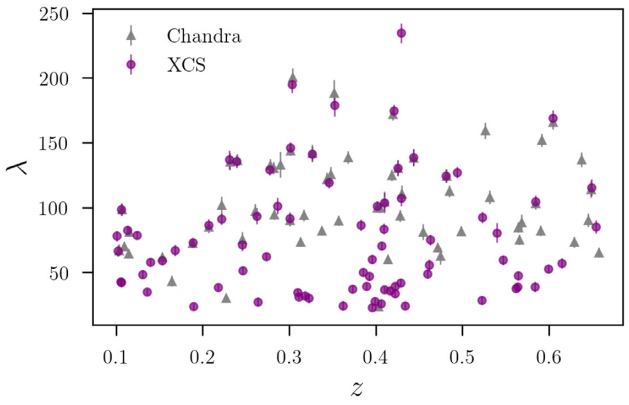

Figure 1. Distribution in richness λ and redshift for the DES Y1 redMaPPer clusters matched to *Chandra* and *XMM* archival data (*XCS* in the figure) using the methods presented in Hollowood et al. (2019) and Giles et al. (in preparation).

template-based Bayesian photometric redshifts (BPZ) algorithm (Benítez 2000). The catalogue used in this work uses the same procedure as outlined in Hoyle et al. (2018). Briefly, six basic templates taken from Coleman, Wu & Weedman (1980) and Kinney et al. (1996) were corrected for redshift evolution and any residual calibration errors. Corrections were performed via finding the best-fitting template for a subset of the PRIMUS spectroscopic data set (Cool et al. 2013) and computing median offsets between the observed photometry and template predictions within each template type, in a sliding redshift interval, $\Delta z = 0.06$. The magnitude and galaxy type redshift prior was then calibrated using the COSMOS + UltraVISTA photometric redshift catalogue of Laigle et al. (2016). Our BPZ run produces redshift probability distributions for $0 < z < 3.5$ in steps of $dz = 0.01$. We use the mean of the probability distribution function (PDF) and an estimate of the width of the PDF: Welch et al. (in preparation) show that this is a good enough approximation to estimate membership probabilities with our method. The member galaxy properties are instead computed assuming the much more precise cluster redshift.

2.1.1 *Completeness of the stellar mass sample*

The galaxy sample described in Section 2.1 is cut in r-band absolute magnitude. Absolute magnitudes were estimated using K-corrections computed from galaxy templates generated by KCORRECT v4.2 (Blanton & Roweis 2007). We took each galaxy's redshift to be the same as its photo-z, found the closest KCORRECT template on a grid of redshift and colours ($g - r$, $r - i$, and $i - z$), and used that template's K-correction from observed i band to rest-frame r band to calculate M_r. An absolute magnitude cut M_r brighter than −19.8 was then applied to the galaxy catalogue. This cut ensures that our galaxy sample is volume limited across the redshift range considered. In Fig. 2, we show the observed r-band magnitudes that the galaxies in our sample would have if they had an absolute magnitude $M_r = -19.8$ as a function of redshift. These are computed using the K-corrections and distance modulus output by our galaxy spectral energy distribution (SED) fitting code using BMA (described in Section 3) for galaxies with a membership probability > 15 per cent (corresponding to the median of the membership probability distribution), in order to be representative of a realistic cluster galaxy population. We show that the 90th percentile of the distribution in redshift bins is below the

[1] www.darkenergysurvey.org
[2] For public data release see: http://des.ncsa.illinois.edu/releases/sva1.
[3] https://github.com/esheldon/ngmix

95 per cent completeness limit of the DES Y1A1 gold catalogue (22.9 in *i* band) over the redshift range covered by the redMaPPer cosmology catalogue. We compare to the Y1 magnitude limit as our galaxy catalogue contains objects detected in Y1, even if they are matched to the deeper Y3 photometry. We can conclude that with the chosen cut we are ~ 90 per cent complete.

In order to estimate the completeness in stellar mass, we look at the mass $M_\star^{\rm lim}$ each galaxy would have, at its redshift, if its absolute magnitude were equal to $M_r^{\rm lim} = -19.8$. This can be achieved by converting the mass-to-light ratio fitted by BMA through $\mathrm{Log}(M_\star^{\rm lim}) = \mathrm{Log}(M_\star) + 0.4(M_r - M_r^{\rm lim})$, where M_r and $M_\star$ are the galaxy estimated absolute magnitude and stellar mass. From Fig. 2 it is clear that, if all the galaxies were at $M_r^{\rm lim}$ or fainter, $\gtrsim 90$ per cent of them would have a stellar mass $\lesssim 10^{10}\,\mathrm{M}_\odot$. We therefore are $\gtrsim 90$ per cent complete above $M_\star = 10^{10}\,\mathrm{M}_\odot$ over the whole redshift range. The scatter in mass at each redshift is given by the scatter in *M*/*L* of the different models. We therefore cut our stellar mass sample at $M_\star > 10^{10}\,\mathrm{M}_\odot$.

2.2 X-ray catalogues

The $\mu_\star$–X-ray mass observable relations are computed using archival *XMM* and *Chandra* data. The DES Y1 redMaPPer cluster catalogue is used to find galaxy clusters in the X-ray data bases at the same positions. Consequently, the samples are not X-ray selected. However, X-ray temperature and luminosity measurements are not available for all of the redMaPPer clusters, either due to a lack of archival observation, or the number of photons is not enough to estimate the luminosity or temperature. In this work, we only focus on temperatures rather than luminosities, since the latter exhibit a larger variance if non-core excised (Fabian et al. 1994; Mantz et al. 2016). Supplemental survey masks would need to be modelled in order to recover the core-excised measurements.

The *XMM* (Jansen & Laine 1997) is a European Space Agency space mission launched in 1999. The *XMM* Cluster Survey (*XCS*) consists in a search for galaxy clusters in archival *XMM–Newton* observations. The DES Y1 redMaPPer sample was matched to all *XMM* ObsIDs (with usable EPIC science data) under the requirement that the redMaPPer position be within 13 arcmin of the aim point of the ObsID. X-ray sources for each ObsID were then detected using the XCS Automated Pipeline Algorithm (XAPA; Lloyd-Davies et al. 2011). At the position of the most likely central galaxy of each redMaPPer cluster, we matched to all XAPA-defined extended sources within a comoving distance of 2 Mpc. Cutout DES and *XMM* images are then produced and visually examined to assign a XAPA source to the optical cluster.

In order to derive the cluster X-ray temperature, we use the *XCS* Post Processing Pipeline (`XCS3P`) as described in Giles et al. (in preparation), and briefly describe the methodology here. Cluster spectra are extracted and fitted using the XSPEC (Arnaud 1996) package, performed in the 0.3–7.9 keV band with an absorbed MeKaL model. The cluster spectra are extracted within r_{2500c}, centred on the XAPA-defined centre of the cluster emission, and estimated through an iterative procedure. An initial temperature is estimated using the XAPA source detection region, and r_{2500c} estimated from the r_{2500c}–kT relation of Arnaud, Pointecouteau & Pratt (2005). For clusters falling on multiple observations, we utilize all available cameras (i.e. PN, MOS1, and MOS2) in a simultaneous fit, provided the individual camera spectral fits are reliable. Cameras are only included in the simultaneous fit if the temperature is within the range 0.08 keV $< T_{\rm X} <$ 30 keV, and contains both upper and lower 1σ errors. The iteration process

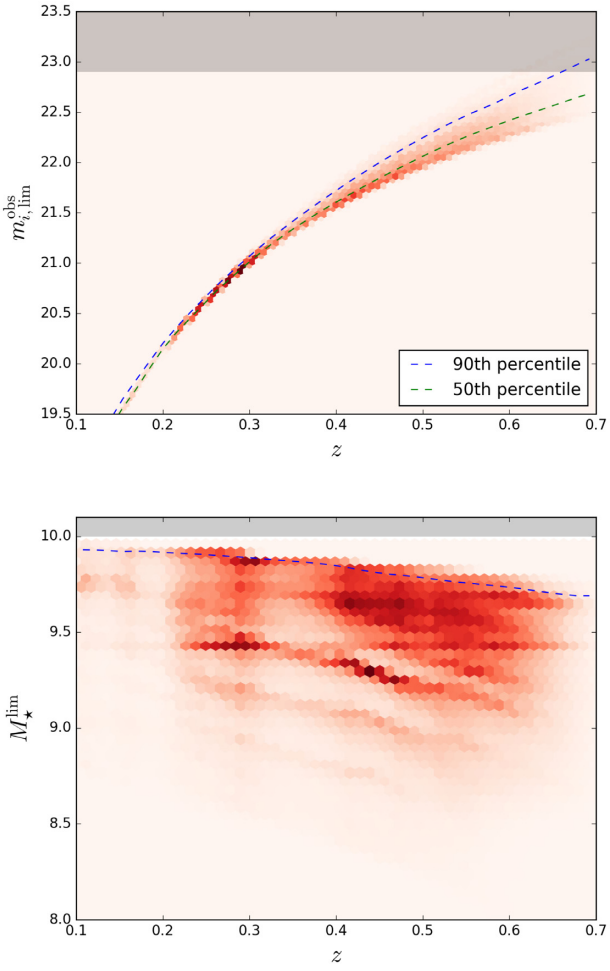

Figure 2. Analysis of the completeness of the galaxy sample. *Top panel:* observed *i*-band magnitudes that the galaxies in our sample would have if they had the absolute magnitude used as our limit ($M_r^{\rm lim} = -19.8$). The bottom edge of the shadowed region represents the DES Y1 95 per cent completeness limit from Drlica-Wagner et al. (2018). *Bottom panel:* limiting mass $M_\star^{\rm lim}$ that each galaxy would have, at its redshift, if its absolute magnitude were equal to $M_r^{\rm lim} = -19.8$. The limiting mass is below $10^{10}\,\mathrm{M}_\odot$ at all redshifts; we therefore cut our sample at this stellar mass. The shadowed region represents this cut. The dashed lines are the 50th and 90th percentile of the distributions.

is performed until r_{2500c} converged to within 10 per cent. To take into account the background, we used a local background annulus centred on the cluster with an inner and outer radius of $2r_{2500}$ and $3r_{2500}$, respectively. All other detected sources in the field, extended and point sources, were excluded from the analysis. However, our detection routine does not exclude point sources at the centre of the extended emission. We do not therefore distinguish these sources from what could be a cool core, and accept this as part of the intrinsic scatter. This could present a problem at high redshift where AGN emission could dominate over the emission, but again we accept this as part of the intrinsic scatter. A recent study in XXL clusters at high redshift ($z \sim 1$) determined that this was not significant for robust extended X-ray source detections (Logan et al. 2018). Furthermore, a calculation of coefficient of variation (Koopmans, Owen & Rosenblatt 1964) of $T_{\rm X}$ is performed, defined as the ratio of the standard deviation (σ) to the mean (μ), given by $C_v = \sigma(T_{\rm X})/\mu(T_{\rm X})$. The values for $\sigma(T_{\rm X})$ and $\mu(T_{\rm X})$ are taken from the

distribution of temperature measurements from all iterations. In this work, we adopt a value of $C_v < 0.25$ as an indicator of a reliable measurement of the iterative temperature, excluding clusters with $C_V > 0.25$ from the sample. The final sample is composed of 58 clusters in the DES Y1 wide field, and the list of clusters is reported in Appendix A.

The *Chandra X-ray Observatory* is a NASA telescope launched in 1999. In order to obtain X-ray temperatures for archival *Chandra* data, we use the Mass Analysis Tool for *Chandra* (MATCha) pipeline, described in Hollowood et al. (2019). This pipeline finds, downloads, and cleans archival *Chandra* data for each of its input cluster candidates. It then iteratively finds a galaxy cluster centre (until converged within 15 kpc), and iteratively fits X-ray temperatures within 500 kpc, r_{2500c}, and r_{500c} apertures (until converged within 1σ). As with XCS3P, MATCha performs its fitting using XSPEC, with an absorbed MeKaL model. As in XCS3P, MATCha performs its fits within the 0.3–7.9 keV band. For consistency between the *XCS* and *Chandra* samples, we apply to both the same SNR > 5 cut. The SNR is defined by the number of counts in a 500 kpc region within the 0.3–7.9 keV energy range, compared to the counts in a background region (taken as an annulus outside of the inner region). A more detailed description of the detection process can be found in Hollowood et al. (2019). We choose to use temperatures within r_{2500c} for this sample because they are more accurate for nearby clusters, where the r_{500c} apertures become too big compared to the *Chandra* chip. Our *Chandra* sample is composed of 64 clusters in the DES Y1 wide field, and the list of clusters used is reported in Appendix A. For comparison, the redMaPPer catalogue used in this work contains 357 and 212 clusters in the *XMM* and *Chandra* fields, respectively.

In order to perform a joint fit between the two X-ray samples and improve our population statistics, we correct for a systematic misalignment between the *Chandra* and *XMM* temperature measurements, as estimated by Rykoff et al. (2016)

$$\mathrm{Log}(T_{\mathrm{X}}^{\mathrm{Chandra}}) = 1.0133\mathrm{Log}(T_{\mathrm{X}}^{\mathrm{XMM}}) + 0.1008\,, \tag{1}$$

where the temperatures are in keV. In the following, we use equation (1) to convert *XMM* temperatures. The calibration relation found in Farahi et al. (2019a) using the same cluster sample used here (apart from a few clusters falling in the supernovae fields, which we did not include in this analysis), has 15 clusters with both *Chandra* and *XMM* temperatures, and is consistent with the relation reported above. In our joint analysis, we use the *Chandra* temperatures, and convert the *XMM* ones to the *Chandra* frame for the remaining clusters using equation (1).

3 METHOD

3.1 Stellar mass estimation

3.1.1 Stellar mass with Bayesian model averaging

A major cause of uncertainty in stellar mass estimation from broad-band photometry is in the model assumptions (see e.g. Mitchell et al. 2013) that are needed in model fitting techniques. These assumptions mainly involve redshift, star formation history (SFH), the initial mass function (IMF), the dust content, and the knowledge of stellar evolution at all stages. Rykoff et al. (2016) showed that the redMaPPer photometric redshifts for DES are excellent, with errors of the order $\sigma_z/(1+z) \sim 0.01$ up to $z \sim 0.9$. This allows us to safely assume the cluster redshift for the cluster members and to avoid exploring the photo-z dependence of stellar masses, as was done in another DES study by Capozzi et al. (2017). Despite the fact that in this work we can safely assume that the cluster redshift is a good estimate of the real galaxy redshift, all the other assumptions remain unconstrained. We therefore choose not to ignore the uncertainty on model selection and use a set of robust, up-to-date stellar population synthesis (SPS) models and average over all of them, marginalizing over the model uncertainty. The method used here is called BMA (see e.g. Hoeting et al. 1999). BMA has already been successfully applied to galaxy SED fitting parameter estimation in Taylor et al. (2011).

Our code can be used to estimate physical parameters of galaxies (stellar masses, specific star formation rates, ages, metallicities) as well as cluster stellar masses and total star formation rate (SFR) when provided with cluster membership probabilities, and it is publicly available at https://github.com/apalmese/BMAStellarMasses.

The BMA starting point is Bayes' theorem, through which we can write the posterior probability distribution $p(\bar{\theta}_k|D, M)$ of the set of parameters $\bar{\theta}_k$ given the data D and the model M_k

$$p(\bar{\theta}_k|D, M_k) = \frac{p(D|M_k, \bar{\theta}_k)p(\bar{\theta}_k|M_k)}{p(D|M_k)}\,, \tag{2}$$

where $p(D|M_k, \bar{\theta}_k)$ is the likelihood, $p(\bar{\theta}_k|M_k)$ is the prior probability of the parameters given the model M_k, and $p(D|M_k)$ is the evidence. In our case, the set of parameters $\bar{\theta}_k$ define the stellar population properties (e.g. stellar mass, SFH parameters, metallicity) of model M_k, and the data D are the galaxy's observed magnitudes.

The model averaged posterior distribution of the parameters $\bar{\theta}_k$ is given by the sum of the single model M_k posteriors, weighted by the model prior

$$p(\bar{\theta}_k|D) = \frac{\sum_k p(\bar{\theta}_k|D, M_k)p(M_k)}{\sum_k p(M_k|D)}\,. \tag{3}$$

From BMA it also follows that the posterior distribution of a quantity Δ is the average of the single model posteriors for that quantity, weighted by their posterior model probability

$$p(\Delta|D) = \sum_k p(\Delta|D, M_k)p(M_k|D)\,. \tag{4}$$

The posterior model probabilities can be computed by

$$p(M_k|D) = \frac{p(D|M_k)p(M_k)}{\sum_k p(D|M_k)p(M_k)}\,, \tag{5}$$

where

$$p(D|M_k) = \int p(D|M_k, \bar{\theta}_k)p(\bar{\theta}_k|M_k)\mathrm{d}\bar{\theta}_k\,. \tag{6}$$

In our case, $p(\bar{\theta}_k|M_k)$ is simply a delta function, as the parameters $\bar{\theta}_k$ (i.e. the SFH parameters, metallicities, etc.) fully define our models M_k.

From equation (6), one can write

$$\langle\Delta\rangle = \sum_k \bar{\Delta}_k p(M_k)\mathcal{L}_k\,, \tag{7}$$

where $\bar{\Delta}_k$ is the mean Δ value from the model M_k, which is defined by the set of parameters $\bar{\theta}_k$ including metallicity and SFH parameters. $\mathcal{L}_k$ is the likelihood $p(D|M_k)$ that we will reconstruct from the χ^2 distribution. The model prior $p(M_k)$ is uniform over all models.

In our code, the mass-to-light ratio $M_\star/L$ is the quantity Δ. Its posterior mean over all the models considered is then used to

Table 1. Parameters of the models used in the BMA SED fitting.

Parameter	Values
Z	0.03, 0.019, 0.0096, 0.0031
t_i (Gyr)	0.7, 1.0, 1.5, 2.0
t_t (Gyr)	7, 9, 11, 13
τ (Gyr)	0.3, 1.0, 1.3, 2.0, 9.0, 13.0
θ (deg)	−10, −20, −30, −40, −50, −80

estimate the stellar mass $M_\star$ of each single galaxy through

$$\mathrm{Log}(M_\star/M_\odot) = \langle M_\star/L\rangle - 0.4(i - DM + \langle kii\rangle - 4.58)\,, \quad (8)$$

where $\langle M_\star/L\rangle$ is the weighted mean stellar mass-to-light ratio in solar mass units, i is the observed i-band magnitude, DM is the distance modulus, $\langle kii\rangle$ is the weighted mean of the K-correction $i_{\mathrm{restframe}} - i$, and 4.58 is the i-band absolute magnitude of the Sun. Weighted means are considered over all models.

In this work, we use the flexible stellar population synthesis (FSPS) code by Conroy & Gunn (2010) to generate simple stellar population spectra. Those are computed assuming Padova (Girardi et al. 2000, Marigo & Girardi 2007, Marigo et al. 2008) isochrones and Miles (Sánchez-Blázquez et al. 2006) stellar libraries with four different metallicities ($Z = 0.03$, 0.019, 0.0096, and 0.0031). We choose the four-parameter SFH described in Simha et al. (2014)

$$\mathrm{SFR}(t) = \begin{cases} A(t - t_i)\mathrm{e}^{(t-t_i)/\tau} & \text{if } t < t_t \\ \mathrm{SFR}(t_t) + \Gamma(t - t_t) & \text{otherwise} \end{cases}, \quad (9)$$

where t_i is the time at which star formation commences (∼1 Gyr), t_t is the time when the SFR transitions from exponential to a linear fall off (∼9 Gyr), τ is the exponential time-scale, and Γ is the slope of the linearly decreasing SFR as a function of time t after t_t. Defining θ as $\Gamma \equiv \tan\theta$, we make the four parameters vary on a grid of values within the following ranges: $\tau \in [0.3, 13]$ Gyr, $t_i \in [0.7, 2]$ Gyr, $t_t \in [7, 13]$ Gyr, and $\theta \in [-10, -80]$ deg. Table 1 reports the grid of values used for these parameters.

For each observed galaxy, we construct the likelihood $\mathcal{L}_k$ in equation (7) as $\mathcal{L}_k \propto e^{-\chi_k^2/2}$, with

$$\chi_k^2 = \sum_j \frac{(C_i - C_{k,j})^2}{\sigma_{C_j}^2}\,, \quad (10)$$

where the sum is over the colours $g - r$, $r - i$, and $i - z$. C_j are the observed colours, while $C_{k,j}$ are the colours predicted by the model M_k for the colour j. The scaling for the theoretical model is given by the i-band filter. σ_{C_j} are the observed errors added in quadrature with a lower limit of 0.02.

3.1.2 *Validation of the BMA method*

In order to test our method for stellar mass estimation, we use as reference a catalogue that overlaps with DES observations. Laigle et al. (2016) used LEPHARE to compute stellar masses with multiband data in 16 filters from UV to infrared over the 2 deg^2 COSMOS field. From this sample, matched to DES data, we remove all objects at $z = 0$ to eliminate stars, and at $z > 1.5$, as higher redshift galaxies are beyond the interests of this work. Galaxies with i-band magnitude above 23.0 are also cut out. The remaining sample comprises galaxies with SNR > 10 in DES, for which we compute stellar masses using the BMA code and DES data. The bias distribution given by the difference in log galaxy stellar mass between the two samples $\mathrm{Log}(M_\star^{\mathrm{COSMOS}}) - \mathrm{Log}(M_\star^{\mathrm{BMA}})$ is shown in Fig. 3. Mean bias and scatter (that we quantify as the standard deviation of the distribution) are below the typical error on galaxy stellar masses from SED fitting (∼0.2 dex) in the redshift range $0.2 < z < 0.6$, where we expect good performance for optical surveys such as DES. At higher redshift, it is harder to constrain the optical to near-infrared (NIR) SED with the DES bands and therefore the scatter increases. Also at low redshifts ($z < 0.2$), the 4000 Å break is harder to constrain, as it is blueward of the g-band effective wavelength. The ∼0.1 dex bias that can be seen from Fig. 3, particularly towards higher redshift, is mostly due to the degeneracies between stellar mass and dust extinction. In fact, we find that the bias is almost null for passive, mostly dust-free galaxies, while it is more pronounced for star-forming dusty galaxies. Because our set-up does not include dust, the resultant masses are biased high (because the presence of dust makes them redder). Including dust in our models would introduce further systematics since our wavelength coverage does not extend to rest-frame infrared wavelengths, particularly at higher redshifts. Laigle et al. (2016) are able to constrain dust extinction because of the information brought by the infrared data available to them. Overall, differences between the two catalogues will also be partially due to the fact that the COSMOS stellar masses are not 'true' stellar masses, and will depend on the assumptions and methodology in Laigle et al. (2016). Among those assumptions, the synthetic templates assumed by Laigle et al. (2016) are from Bruzual & Charlot (2003), and thus will differ from the models assumed here. We conclude that the observed bias is due to a choice of templates, rather than to the BMA method itself.

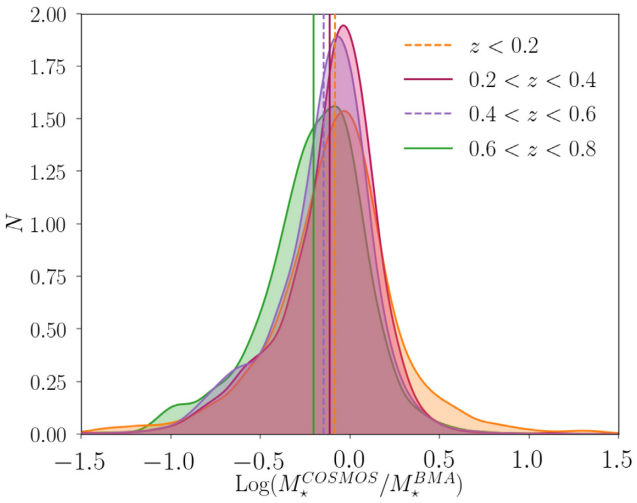

Figure 3. Comparison of galaxy stellar masses from Laigle et al. (2016) using COSMOS data with those computed with the BMA algorithm using DES data in different redshift bins. The lines represent the mean value of the distributions with the same colour. The histograms have been smoothed with a Gaussian kernel for visualization purposes, and arbitrarily renormalized. The total number of galaxies used is ∼ 120 000.

One of the main advantages of the BMA method is that it allows to formally incorporate the model uncertainty into the stellar mass uncertainty. This is particularly important for star-forming galaxies. As it turns out from the discussion above, stellar mass estimates of red and passive galaxies are found to be more robust. We find that the uncertainties derived from BMA for this type of galaxy are comparable to those from a more standard approach such as the one adopted in LEPHARE, using a similar set of templates and the same input magnitudes. On the other hand, blue star-forming galaxies uncertainties are larger by a factor 1.5–2, reflecting the fact that there are a number of models that could similarly fit that data.

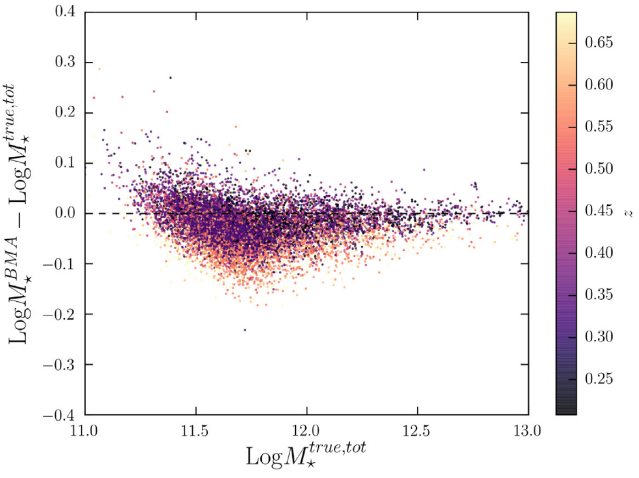

Figure 4. Comparison of BMA clusters stellar mass to Millennium simulation true values at different redshifts. The dashed lines indicate no difference between the BMA estimates and the true values.

We also test our results against the Millennium simulation semi-analytic model from De Lucia & Blaizot (2007),[4] and show the results for the sum of stellar mass in clusters (selected as haloes with $M_{200c} > 10^{14}$ $\mathrm{M}_\odot$), in Fig. 4. We run the BMA algorithm using the simulated magnitudes for the *griz* SDSS filters, which are very similar to the DES ones. In this case, the scatter of the bias distribution is even lower (standard deviation is ∼0.04 dex) than what found in the comparison with the COSMOS results, showing that our method works well against other SED fitting methods and simulations.

3.2 From galaxy stellar masses to $\mu_\star$

The cluster mass proxy $\mu_\star$ is computed by weighing the stellar mass of each galaxy in the cluster by its membership probability $p_{\mathrm{mem},\,i}$

$$\mu_\star = 10^{-10}\,\mathrm{M}_\odot^{-1} \sum_i p_{\mathrm{m},i}\,M_{\star,i}\,, \tag{11}$$

where the factor 10^{-10} simply gives to the mass proxy an order of magnitude similar to that of the number of observed cluster galaxies. The sum is over all the galaxies from the DES Y1A1 gold catalogue having $M_r < -19.8$ and within 3 Mpc from the centre of the cluster as given by the redMaPPer Y1 catalogue. The membership probability is computed as described in Welch et al. (in preparation), where the membership assignment scheme is presented in detail, together with measurements of the red sequence for redMaPPer clusters. The probability is given by

$$p_\mathrm{m} = p_\mathrm{R}\,p_z\,, \tag{12}$$

where the components represent the probability of the galaxy being a member given its redshift (p_z) and its distance from the cluster centre (p_R). The radial probability p_R is assigned by assuming a projected Navarro–Frenk–White (NFW; Navarro, Frenk & White 1996) profile, with R_{200c} computed by counting galaxies within 3 Mpc and finding the halo profile by assuming a halo occupation distribution (HOD) model. The redshift probability p_z is computed by comparing the photo-z $p(z)$ of single galaxies to the cluster redshift. The membership probability presented here differs from the one provided by redMaPPer because it uses photometric redshift information, instead of a red-sequence calibration. The computation of the radial probability is similar, as it assumes the same function for the galaxy profile, while the radius may be different as our method utilizes the HOD model.

We also provide a colour probability p_c, the probability that a galaxy belongs to either the red sequence or the blue cloud given its colour. This is estimated through a Gaussian mixture model (GMM) similar to Hao et al. (2009). This method fits two Gaussians to the colour distribution of the galaxies in each cluster, weighted by their radial and redshift probabilities. The Gaussians fit the colour distribution of the red sequence and blue cloud of cluster galaxies well. The area of the Gaussians w_red and w_blue satisfies $w_\mathrm{red} + w_\mathrm{blue} = 1$ and is used to compute the colour probability

$$p_\mathrm{c} = w_\mathrm{red}\,p_\mathrm{red} + w_\mathrm{blue}\,p_\mathrm{blue}\,, \tag{13}$$

where p_red (p_blue) is the probability that a galaxy belongs to the red sequence (blue cloud) given its colour and the GMM estimates. The cluster colour distribution is derived after a local background subtraction is performed by measuring the colour distribution of galaxies in the cluster outskirts (between 3 and 5 Mpc). This is done for the colours $g - r$, $r - i$, and $i - z$. The inclusion of the colour probability as an extra term multiplied to the right-hand side of equation (12) is tested in Section 4. See Welch et al. (in preparation) for a full description of the membership probability scheme.

The errors on $\mu_\star$ were computed using jackknife resampling. Intuitively, this method allows us to estimate the variance on our estimator by considering a galaxy cut from the cluster at each time.

We note that the impact of the stellar mass bias seen in Fig. 3 for COSMOS galaxies does not have a significant effect on $\mu_\star$. In fact, the bias is reduced to 0.05 dex for a sample of galaxies such as those used in this work for Y1 clusters ($M_\star > 10^{10}$ $\mathrm{M}_\odot$, $z < 0.7$), with most of the contribution coming from star-forming galaxies. If we assume that the star-forming galaxies can constitute up to ∼ 30 per cent of cluster galaxies in number, and that their typical masses are $10^{10.5}$ $\mathrm{M}_\odot$ (versus $10^{10.7}$ $\mathrm{M}_\odot$ of the passive galaxies, as computed from the COSMOS $M_\star > 10^{10}$ $\mathrm{M}_\odot$, $z < 0.7$ sample), the maximum bias introduced on $\mu_\star$ is 2.6 per cent, which is well below the typical 10 per cent errors in $\mu_\star$.[5] In reality, this upper bound is further reduced by the radial membership probabilities p_R, because the passive, red-sequence galaxies dominate in the centre of clusters (e.g. Mahajan & Raychaudhury 2009).

3.3 Hot gas temperature–stellar mass relations

Following previous works (e.g. Rozo et al. 2009a; Rozo et al. 2011; Evrard et al. 2014; Farahi et al. 2019a; Mulroy et al. 2019), we assume that the likelihood of a cluster to have a true value of the X-ray temperature T^tr, given that it has a stellar mass true value $\mu_\star^\mathrm{tr}$, is a lognormal function. Following the notation in Evrard et al.

[4] http://gavo.mpa-garching.mpg.de/Millennium/Help?page = databases/millimil/delucia2006a

[5] Note that up to ∼ 30 per cent of cluster galaxies are blue (Zu & Mandelbaum 2016), but not necessarily star forming. Even if most blue galaxies are star forming compared to red-sequence galaxies, there exist a smaller fraction of blue galaxies which are passive, and red galaxies that are sta forming (e.g.Mahajan & Raychaudhury 2009). However, even if we assumed a conservative fraction of 50 per cent for the content of star-forming galaxies in clusters, the expected upper limit (∼ 4.7 per cent) of the bias would still be below our uncertainties.

Table 2. Scaling relation parameters from this work following equation (15) for X-ray temperatures. The upper part of the table shows our results for the temperature over the whole $0.1 < z < 0.7$ redshift range. The bottom section presents results in different redshift bins for the temperatures from the joint *Chandra* + *XMM* sample. Values represent the median of the parameters posterior distribution, and the errors are the 16th and 84th percentiles. Temperatures are in units of keV.

Sample	$\pi_{\ln T_X\|\mu_\star}$	$\alpha_{\ln T_X\|\mu_\star}$	$\sigma_{\ln T_X\|\mu_\star}$	$\ln(\tilde{\mu}_\star)$
XMM	$1.306^{+0.035}_{-0.035}$	$0.449^{+0.054}_{-0.055}$	$0.277^{+0.026}_{-0.029}$	6.61
Chandra	$1.887^{+0.032}_{-0.032}$	$0.463^{+0.072}_{-0.072}$	$0.229^{+0.025}_{-0.027}$	7.07
Chandra + *XMM*	$1.711^{+0.024}_{-0.025}$	$0.488^{+0.043}_{-0.043}$	$0.266^{+0.019}_{-0.020}$	6.85
Chandra + *XMM* ($z < 0.3$)	$1.781^{+0.041}_{-0.042}$	$0.501^{+0.084}_{-0.084}$	$0.262^{+0.029}_{-0.033}$	6.79
Chandra + *XMM* ($0.3 < z < 0.5$)	$1.753^{+0.035}_{-0.036}$	$0.497^{+0.056}_{-0.055}$	$0.263^{+0.027}_{-0.031}$	7.03
Chandra + *XMM* ($z > 0.5$)	$1.682^{+0.066}_{-0.065}$	$0.54^{+0.13}_{-0.14}$	$0.311^{+0.051}_{-0.064}$	6.91

(2014) and Farahi et al. (2019a):

$$P(T^{\rm tr}|\mu_\star^{\rm tr}, z) = \frac{1}{\sqrt{2\pi}\sigma_{\ln T|\mu_\star}} \exp\left[-\frac{(\ln T^{\rm tr} - \langle \ln T^{\rm tr}|\mu_\star^{\rm tr}, z\rangle)^2}{2\sigma^2_{\ln T|\mu_\star}}\right], \tag{14}$$

where $\sigma_{\ln T|\mu_\star}$ is the intrinsic scatter of the hot gas temperature at fixed stellar mass, $\mu_\star^{\rm tr}$. We perform a Bayesian linear regression (Kelly 2007) to estimate a linear relation between the logarithm of the X-ray temperature and the logarithm of stellar mass. The free parameters include normalization, slope, and the scatter about the mean relation. Namely, we fit

$$\langle \ln T|\mu_\star, z\rangle = \left[\pi_{T|\mu_\star} + \frac{2}{3}\ln(E(z))\right] + \alpha_{T|\mu_\star} \ln\left(\frac{\mu_\star}{\tilde{\mu}_\star}\right), \tag{15}$$

where $\tilde{\mu}_\star$ is the median $\mu_\star$ of the sample and $E(z) = H(z)/H_0$ is the Hubble parameter evolution. The normalization term containing $E(z)$ takes into account the redshift dependence of the temperature, as expected for a self-similar evolution of the intracluster medium in virial equilibrium (Kaiser 1991; Bryan & Norman 1998). We use the publicly available PYTHON version of Kelly (2007) to perform this regression, which provides samples from the posterior distribution of the normalization, $\pi_{T|\mu_\star}$, slope, $\alpha_{T|\mu_\star}$, and scatter about the mean relation, $\sigma_{\ln T|\mu_\star}$. The regression code takes into account uncertainties associated with both the dependent and independent variables by assuming a mixture model. Such errors are assumed to be lognormal, and they are transformed to lognormal space through $\sigma_{\ln T} = \sigma_T/T$.

3.4 Mass scatter inference

We follow Evrard et al. (2014) and Farahi et al. (2019a) model to infer the halo mass scatter at fixed $\mu_\star$. Evrard et al. (2014) proposed a population model that computes a closed form solution for conditional properties of an observable, here $T_{\rm X}$, given a selection observable, here stellar mass $\mu_\star$, as a function of their halo properties. We employ their model to infer the halo mass scatter. In the following, we denote the log of halo mass by $\ln M$. According to their population model, the scatter in temperature at fixed $\mu_\star$ can be written as

$$\frac{\sigma^2_{\ln T|\mu_\star}}{\alpha^2_{T|M}} = \left[\sigma^2_{\ln M|\mu_\star} + \sigma^2_{\ln M|T} - 2r_{\mu_\star T}\sigma_{\ln M|\mu_\star}\sigma_{\ln M|T}\right]. \tag{16}$$

We employ $\sigma_{\ln M|T} = \sigma_{T|\ln M}/\alpha^2_{T|M}$ and solve for $\sigma_{\ln M|\mu_\star}$, which is the quantity of interest. After rearrangement, the solution yields

$$\sigma^2_{\ln M|\mu_\star} = \sigma^2_{\ln M|T}\left[\left(\frac{\sigma^2_{\ln T|\mu_\star}}{\sigma^2_{\ln T|M}} - (1 - r^2_{\mu_\star T})\right)^{1/2} + r^2_{\mu_\star T}\right]^2, \tag{17}$$

where $r_{\mu_\star T}$ is the correlation coefficient between $\mu_\star$ and temperature deviations about their mean values at fixed halo mass. The values used for $r_{\mu_\star T}$ and $\sigma^2_{\ln T|M}$ will be discussed in Section 4.3.

4 RESULTS AND DISCUSSION

4.1 X-ray scaling relations

We first fit the scaling relation presented in Section 2.2 for the *XMM* and *Chandra* samples separately. The results of the regression are reported in Table 2 and shown in Fig. 5. A few outliers are clearly visible in both samples, particularly in the low-$T_{\rm X}$ regime. Only one data point (shown in lighter grey in Fig. 5) has a significant deviation from the mean relation ($> 3\sigma_{\ln T|\mu_\star}$), and it has been excluded from the regression. These outliers tend to have a higher $\mu_\star$ than expected from the mean scaling relation. It is likely that these estimates are affected by the presence of structure along the line of sight, which boosts the mass proxy value. A similar behaviour is also found in Farahi et al. (2019a) for the same clusters for the redMaPPer richness, which is computed through a very different methodology, meaning that the outliers are likely related to the galaxies in the DES catalogue rather than to the method.

We have tested the dependence of the scaling relation results on the completeness of the cluster catalogue. In fact, the X-ray catalogue is likely to be incomplete at the low-temperature end. Farahi et al. (2019a) find that the X-ray matched redMaPPer catalogue is ∼50 per cent complete at $\lambda \sim 100$. This corresponds to $\mu_\star \sim 1000$ based on the stellar mass–richness relation found in Palmese et al. (in preparation). We find that, cutting our cluster sample at $\mu_\star > \mu_\star^{\rm cut} = 1000$ or higher values, provides scaling relation constraints that are less stringent than those reported in Table 2, but still consistent within 1σ.

The weak lensing mass–$\mu_\star$ relation studied in Pereira et al. (2018) shows a steeper slope (1.74 ± 0.62 at $0.1 < z < 0.33$ for SDSS redMaPPer clusters) than the analysis presented here. We believe that the correlation of stellar mass with total cluster mass is higher than with the X-ray temperatures because the X-ray measurement only probes the inner part of the cluster gravitational potential (within R_{500c} and R_{2500c} for the *XMM* and *Chandra* data, respectively), while the weak lensing probes larger radii, thus correlating better with the total stellar mass content.

4.2 Intrinsic temperature scatter

We find an intrinsic scatter in temperature at fixed $\mu_\star$ of $\sigma_{\ln T_X|\mu_\star} = 0.277^{+0.026}_{-0.029}$ for the *XCS* sample. This value is consistent with the value found for the redMaPPer optical richness (0.289 ± 0.025)

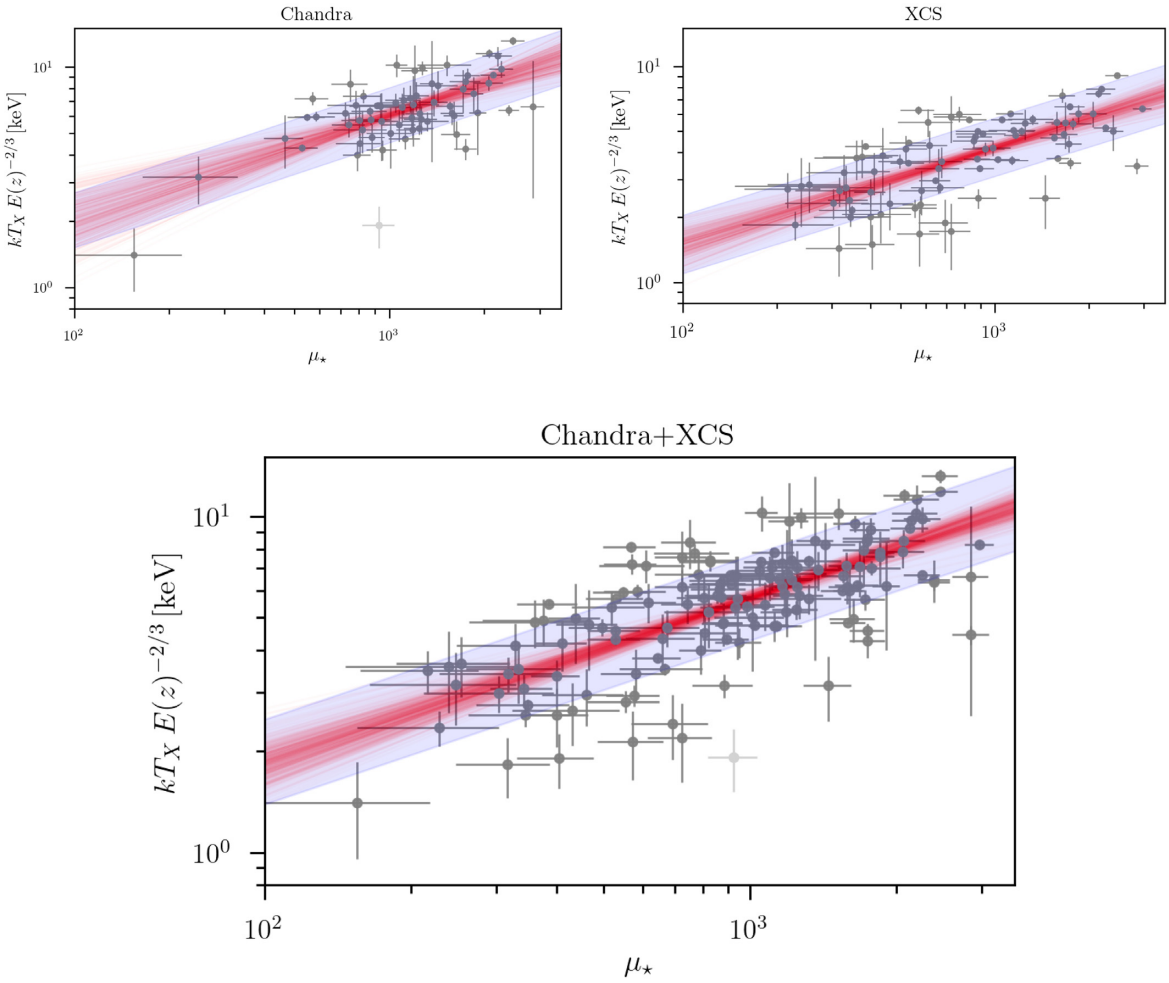

Figure 5. Bayesian linear regression of *X*-ray temperature and $\mu_\star$ for the *Chandra* and XMM samples (top panels) and for the joint sample (bottom panel). The red lines are a random sample from the posterior distribution of slope and intercept, and the blue band represents 1σ around the mean value of the intercept plus the intrinsic scatter. The light grey point has been excluded from the regression because it is an outlier with significant deviation from the mean relation ($> 3\sigma_{\ln T|\mu_\star}$).

in Farahi et al. (2019a) within 1σ.[6] The scatter on ln T_X from the *Chandra* sample is even lower ($0.229^{+0.025}_{-0.027}$) and it is also consistent with the redMaPPer richness estimate (0.260 ± 0.032) within 1σ. The joint scatter for the two samples is $0.266^{+0.019}_{-0.020}$. The redMaPPer richness is an optimized *count* observable, and the stellar mass observable has a consistent scatter. We expect $\mu_\star$ to be affected by projection effects similarly to λ (as described in Costanzi et al. 2019) or somewhat worse (if the photo-z's do not perform well). It should thus have similar or smaller scatter on the basis of individual haloes than is possible from counts alone.

We perform a number of tests to understand if the membership probabilities are taken into account in an optimal way. We find that including the blue cloud galaxies does not bring a significant increase in the scatter: the inclusion of the second term in the right-hand side of equation (13), compared to having solely the red-sequence term or redMaPPer members, brings an additional scatter which is an order of magnitude smaller than the error on that scatter. This is consistent with what we would expect for this sample, as it has been matched to a red-sequence cluster finder. Rozo et al. (2011) found that the blue galaxies significantly increase the scatter of their sample, but the fact that this is not true in our case allows us to keep this contribution which may become relevant at low-richness and high-redshift regimes, which should be tested using a non-red-sequence based cluster finder and matched against other mass observables. It is beyond the scope of this work to test this hypothesis. Rozo et al. (2011) also show that differences between the true and predicted scatter of the mass proxy–mass relation are irrelevant for a DES-like survey as long as these differences are about 5 per cent or less (i.e. $\Delta\sigma < 0.05$), which further supports our choice.

We also test the effect of the probability p_R in equation (12) on $\mu_\star$. We find that the inclusion of this terms makes the mass proxy robust against an arbitrary radial cut between 1 and 4 Mpc: in fact, the intrinsic scatter of the temperature–$\mu_\star$ relation is insensitive to this choice. On the other hand, we tested the use of the red galaxies only without including the radial probability contribution. In this case, we find similar trends to previous work (e.g. Andreon 2015): optimal choices for the aperture *do* exist when no membership probability is considered. We find that the scatter can decrease with increasing radius, by a factor of up to ~ 15 per cent with respect to considering the central galaxy only. The maximum improvement is

[6] σ here refers to the error on the scatter.

found within a radius typically <1.5 Mpc, and outside that radius mostly background/foreground galaxies are added, and the scatter increases with increasing radius.

We tested the inclusion of colour probabilities p_c in the full membership probabilities by modifying equation (12) into $p_m = p_R p_z p_c$. We also tried to combine the colour membership probabilities from different colours in different redshift ranges. This is justified by the fact that most of the colour information in a galaxy SED is contained in the 4000 Å break, that shifts between the bands with redshift. We therefore use $g - r$ for the range $z < 0.35$ and $r - i$ in $z > 0.35$. We find that these tests did not have a significant impact on the mean scaling relation fit and intrinsic scatter, so it is reasonable to include the simpler version of the full probabilities as given in equation (12).

The fact that our scaling relation scatter and slope are insensitive to the choices made in these tests shows that the membership probabilities are robust and that cluster size and colours (that enter in p_m through the redshift probability estimation) are taken into account well.

In order to test the redshift dependence of the scaling relation, we split the joint cluster sample into three subsamples ($z < 0.3$, $0.3 < z < 0.5$, and $z > 0.5$) and perform the same linear regression presented above over the whole redshift range. Slope, intercept, and scatter are all consistent over the different redshift bins. We conclude that we find no evidence for a redshift evolution of the scaling relation out to $z < 0.7$. We believe that this result is related to the fact that the stellar mass content of galaxy clusters is mostly formed before redshift $\sim$1, and it is consistent with other results (e.g. Chiu et al. 2018) and simulations (Farahi et al. 2018).

4.3 Total mass scatter

In order to estimate the scatter in mass at fixed $\mu_\star$ presented in equation (17) we need to have an estimation of the correlation coefficient $r_{\mu_\star T}$, the scatter in temperature at fixed total mass and the scatter in mass at fixed temperature. The correlation coefficient of pairs of nine observables is estimated by Farahi et al. (2019b) by employing multiwavelength analysis of 41 X-ray selected cluster from the LoCuSS clusters sample (Mulroy et al. 2019).[7] We employ their L_K–T_X correlation coefficient which serves as a good approximation of the stellar mass–temperature correlation in our sample. Their posterior estimate of the correlation coefficient is $r_{\mu_\star T} = -0.43^{+0.49}_{-0.35}$. Note that this posterior has support over the whole range of possible values ([− 1, 1]), hence the very broad 1σ interval reported here. Since this posterior only excludes the extreme tails which are not physically realistic, we believe that it is reasonable to use this correlation coefficient estimate in our analysis, despite the fact that the details in the derivation of temperatures and the redshift range (extending only out to $z \sim 0.3$) in Mulroy et al. (2019) may differ from what described here. The additional parameters needed in equation (17), namely $\sigma_{\ln T|M}$ and $\sigma_{\ln M|T}$, are taken from the recent constraints on the scaling relation between the temperature and total mass from weak lensing for the Weighing the Giants program (Mantz et al. 2015, 2016). Their posterior constraints read $\sigma_{\ln T|M} = 0.16 \pm 0.02$ and $\alpha_{T|M} = 0.62 \pm 0.4$. We employ $\sigma_{\ln M|T} = \sigma_{\ln T|M}/\alpha_{T|M}$ to get an estimate of mass scatter at fixed X-ray temperature. The posterior distribution of $\sigma_{\ln M|\mu_\star}$ is then obtained by Monte Carlo sampling the right-hand side of equation (17).

[7]The full posterior chains are publicly available in a figshare repository, https://doi.org/10.6084/m9.figshare.8001218.

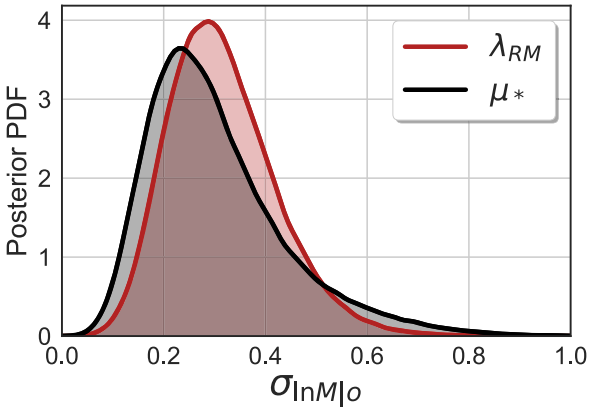

Figure 6. Posterior distribution of the scatter in total mass at fixed mass observable o ($\mu_\star$ in black and λ in red) for the joint cluster sample. In this work, we find $\sigma_{\ln M|\mu_\star} = 0.26^{+0.15}_{-0.10}$.

Table 3. Parameters used to estimate the mass scatter in equation (17) (upper part of the table), and results from this work (lower table).

Parameter	Value	Sample
$\sigma_{\ln T\|M}$	0.16 ± 0.02	Weighing the Giants
$\alpha_{T\|M}$	0.62 ± 0.04	Weighing the Giants
$r_{\mu_\star T}$	$-0.43^{+0.49}_{-0.35}$	LoCuSS
$\sigma_{\ln M\|\mu_\star}$	$0.19^{+0.15}_{-0.09}$	*Chandra*
$\sigma_{\ln M\|\mu_\star}$	$0.28^{+0.16}_{-0.11}$	*XMM*
$\sigma_{\ln M\|\mu_\star}$	$0.26^{+0.15}_{-0.10}$	*Chandra* + *XMM*

The result for the joint X-ray sample is shown in Fig. 6. For the *Chandra* and *XMM* samples, we find $\sigma_{\ln M|\mu_\star} = 0.19^{+0.15}_{-0.09}$ and $0.28^{+0.16}_{-0.11}$, respectively, while from the joint analysis $\sigma_{\ln M|\mu_\star} = 0.26^{+0.15}_{-0.10}$. A summary of the parameters used and of these results is reported in Table 3. The errors on the scatter are dominated by the uncertainty on the external parameters described above. In fact, Fig. 7 shows that the marginalization over the temperature–mass relation (red line) and over the correlation coefficient (yellow line) has a very similar impact on the final posterior estimate, and they dominate the final uncertainty compared to a marginalization over $\sigma_{\ln T|\mu_\star}$ only.

The scatter found here is consistent with what Farahi et al. (2019a) find for the redMaPPer richness. The slight difference is mostly driven by the lower scatter in temperature at fixed $\mu_\star$ described in Section 4.2 for the *Chandra* sample. We believe that there is room for further improvement through a more precise estimation of the correlation coefficient, which is driving the more extended tail in Fig. 6 for $\mu_\star$ compared to the richness case.

We note that generalization of these mass scatter findings to clusters with low temperature, $\mu_\star$ or mass should be taken with caution. Even if our sample is optically selected, we still require a detection in X-ray, with some SNR cut. As a result, both our X-ray sample and the Mantz et al. (2016) sample cover the high-temperature end of the scaling relations. Moreover, Mantz et al. (2016) exclude the cores when measuring X-ray temperatures: it is thus possible that their scatter is smaller than what is applicable to this work. In order to test the effect of different *T*–*M* scatter and scaling relations on our results, we have assumed different scaling relation measurements to derive the mass scatter at fixed $\mu_\star$. In

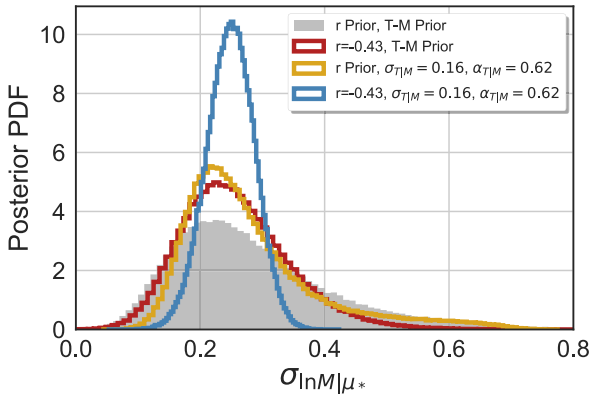

Figure 7. Posterior distribution of the scatter in total mass at fixed $\mu_\star$ for the joint cluster sample, showing the impact of different uncertainties on the final PDF. The grey region corresponds to the grey PDF in Fig. 6. The other lines show the same pdf, when some of the parameters in the right-hand side of equation (17) are fixed to a known value, and the others are allowed to vary. The red line assumes that the correlation coefficient is fixed at $r_{\mu_\star T} = -0.43$, while the yellow line is computed by fixing the slope and scatter in the *T*–*M* relation. The blue line fixes all those quantities, except for the T–$\mu_\star$ scatter derived in this work.

particular, we used the results from Mahdavi et al. (2013) and Lieu et al. (2016), who find a lower and larger scatter than Mantz et al. (2016), respectively. Since the uncertainties on the scaling relation from these works are larger than those from Mantz et al. (2016), the derived mass scatter constraints are weaker, but all consistent with each other. Regardless of the specific value measured for $\sigma_{\ln M|\mu_\star}$, which depends on the analysis choices, one of the main results of this work still holds: the scatter found for this newly established proxy is comparable with the λ measurement.

Remarkably, the scatter found in this work is also consistent with what Farahi et al. (2018) find for the total cluster mass at fixed stellar mass using BAHAMAS and MACSIS simulations, and a similar approach based on Evrard et al. (2014). We assume that $\mu_\star$ probes well the stellar mass content of clusters from BAHAMAS and MACSIS. For the cluster mass probed here ($M_{200c} \sim 10^{14}\,\mathrm{M}_\odot$), we can derive the stellar mass conditioned scatter in total mass from their results through: $\sigma_{\ln M|\mu_\star} \simeq \sigma_{\mu_\star|\ln M}/\alpha_{\mu_\star} \simeq 0.22$.

5 CONCLUSIONS

In this work, we present a stellar mass-based mass proxy, $\mu_\star$, and its application to DES Y1 redMaPPer clusters using DES Y3 photometry. In particular, we present a code that uses BMA to compute galaxy stellar masses and other galaxy properties. The outputs of this code, along with galaxy membership probabilities presented in a companion paper, are used to estimate our mass proxy. We match Y1 redMaPPer clusters to archival *XMM* and *Chandra* data in order to study the scaling relation of $\mu_\star$ with X-ray temperature. Assuming that the scatter in temperature around the mean of the scaling relation at a given $\mu_\star$ is lognormal, and that the temperature scales linearly with $\mu_\star$ in lognormal space, we find that our mass proxy correlates well with the X-ray temperature, with a low intrinsic scatter. Namely, we find that the slope of the scaling relation is $\alpha_{T|\mu_\star} = 0.488^{+0.043}_{-0.043}$ and the scatter is $0.266^{+0.019}_{-0.020}$ for the joint *XMM* and *Chandra* cluster sample. This scatter is consistent with what is found in a simulation study by Farahi et al. (2018). The scaling relation parameters do not show evidence for a deviation from self-similar evolution.

Constraints on the scaling relation between the temperature and total mass from the Weighing the Giants program by Mantz et al. (2016), along with the luminosity–temperature correlation coefficient estimated by Mulroy et al. (2019) on the LoCuSS sample, are then used to derive the expected scatter on halo mass at fixed $\mu_\star$. We find $\sigma_{\ln M|\mu_\star} = 0.26^{+0.15}_{-0.10}$ for the joint *XMM* and *Chandra* sample. The large uncertainty on this parameter is driven by the marginalization over the temperature–mass relation parameters and over the correlation coefficient. Consistent values are also found with the same analysis for the well-established redMaPPer mass proxy λ, showing that $\mu_\star$ is also a potential mass observable to be employed in cosmological analyses with cluster abundances. As such, the mass scatter constrained in this work could serve as a prior on the scatter assumed in the mass observable–mass relation in a cosmological analysis of DES Y1 redMaPPer clusters employing weak lensing measurements.

It is worth noting that using the stellar mass content of galaxy clusters as mass proxies is empirically and physically motivated, and that measurements of $\mu_\star$ also allow straightforward constraints on the stellar-to-halo connection in clusters. In other words, it allows us to better understand how galaxies evolve in clusters through estimates of their stellar content, while providing a useful tool for cosmological analyses. The other motivation for using this mass proxy rather than galaxy counts is that cluster stellar mass has the potential to be less sensitive to projection effects, one of the main sources of systematics for cluster finders when using photometric data.

Overall, our results show that $\mu_\star$ is a promising low scatter mass proxy, which can be used as an alternative to λ, or in conjunction following the formalism by Evrard et al. (2014), for cosmological and astrophysical analyses with redMaPPer clusters. Future work will also include the development of a new version of the Voronoi–Tessellation cluster finder (Soares-Santos et al. 2011) that integrates this mass proxy into the pipeline (Burgad et al., in preparation).

ACKNOWLEDGEMENTS

AP acknowledges the UCL PhD studentship and the URA Visiting scholar award. AF is supported by a McWilliams Postdoctoral Fellowship. OL acknowledges support from a European Research Council Advanced Grant FP7/291329. SB acknowledges support from the UK Science and Technology Facilities Council via Research Training Grant ST/N504452/1. TOPCAT (Taylor 2005) has been extensively used in this work.

Funding for the DES Projects has been provided by the U.S. Department of Energy, the U.S. National Science Foundation, the Ministry of Science and Education of Spain, the Science and Technology Facilities Council of the United Kingdom, the Higher Education Funding Council for England, the National Center for Supercomputing Applications at the University of Illinois at Urbana-Champaign, the Kavli Institute of Cosmological Physics at the University of Chicago, the Center for Cosmology and Astro-Particle Physics at the Ohio State University, the Mitchell Institute for Fundamental Physics and Astronomy at Texas A&M University, Financiadora de Estudos e Projetos, Fundação Carlos Chagas Filho de Amparo à Pesquisa do Estado do Rio de Janeiro, Conselho Nacional de Desenvolvimento Científico e Tecnológico and the Ministério da Ciência, Tecnologia e Inovação, the Deutsche Forschungsgemeinschaft and the Collaborating Institutions in the Dark Energy Survey.

The Collaborating Institutions are Argonne National Laboratory, the University of California at Santa Cruz, the University of

Cambridge, Centro de Investigaciones Energéticas, Medioambientales y Tecnológicas-Madrid, the University of Chicago, University College London, the DES-Brazil Consortium, the University of Edinburgh, the Eidgenössische Technische Hochschule (ETH) Zürich, Fermi National Accelerator Laboratory, the University of Illinois at Urbana-Champaign, the Institut de Ciències de l'Espai (IEEC/CSIC), the Institut de Física d'Altes Energies, Lawrence Berkeley National Laboratory, the Ludwig-Maximilians Universität München and the associated Excellence Cluster Universe, the University of Michigan, the National Optical Astronomy Observatory, the University of Nottingham, The Ohio State University, the University of Pennsylvania, the University of Portsmouth, SLAC National Accelerator Laboratory, Stanford University, the University of Sussex, and Texas A&M University.

The DES data management system is supported by the National Science Foundation under Grant Number AST-1138766. The DES participants from Spanish institutions are partially supported by MINECO under grants AYA2012-39559, ESP2013-48274, FPA2013-47986, and Centro de Excelencia Severo Ochoa SEV-2012-0234. Research leading to these results has received funding from the European Research Council under the European Union's Seventh Framework Programme (FP7/2007-2013) including ERC grant agreements 240672, 291329, and 306478.

REFERENCES

Abbott T. M. C. et al., 2018, ApJS, 239, 18
Andreon S., 2012, A&A, 548, A83
Andreon S., 2015, A&A, 582, A100
Arnaud K. A., 1996, in Jacoby G. H., Barnes J., eds, ASP Conf. Ser. Vol. 101, Astronomical Data Analysis Software and Systems V. Astron. Soc. Pac., San Francisco, p. 17
Arnaud M., Pointecouteau E., Pratt G. W., 2005, A&A, 441, 893
Benítez N., 2000, ApJ, 536, 571
Bertin E., Arnouts S., 1996, A&AS, 117, 393
Blanton M. R., Roweis S., 2007, AJ, 133, 734
Bradshaw C., Leauthaud A., Hearin A., Huang S., Behroozi P., 2020, MNRAS, 493, 337
Bruzual G., Charlot S., 2003, MNRAS, 344, 1000
Bryan G. L., Norman M. L., 1998, ApJ, 495, 80
Butcher H., Oemler A., Jr, 1978, ApJ, 226, 559
Butcher H., Oemler A., Jr, 1984, ApJ, 285, 426
Capozzi D. et al., 2017, preprint (arXiv:1707.09066)
Chiu I. et al., 2018, MNRAS, 478, 3072
Coleman G. D., Wu C.-C., Weedman D. W., 1980, ApJS, 43, 393
Conroy C., Gunn J. E., 2010, ApJ, 712, 833
Cool R. J. et al., 2013, ApJ, 767, 118
Costanzi M. et al., 2019, MNRAS, 482, 490
De Lucia G., Blaizot J., 2007, MNRAS, 375, 2
Desai S. et al., 2012, ApJ, 757, 83
Diehl H. T. et al., 2014, in Peck A. B., Benn C. R., Seaman R. L., eds Proc. SPIE Conf. Ser. Vol. 9149, Observatory Operations: Strategies, Processes, and Systems V. SPIE, Bellingham, p. 91490V
Donahue M. et al., 2002, ApJ, 569, 689
Drlica-Wagner A. et al., 2018, ApJS, 235, 33
Evrard A. E., Arnault P., Huterer D., Farahi A., 2014, MNRAS, 441, 3562
Fabian A. C., Crawford C. S., Edge A. C., Mushotzky R. F., 1994, MNRAS, 267, 779
Farahi A., Evrard A. E., McCarthy I., Barnes D. J., Kay S. T., 2018, MNRAS, 478, 2618
Farahi A. et al., 2019a, MNRAS, 490, 3341
Farahi A. et al., 2019b, Nat. Commun., 10, 2504
Flaugher B. et al., 2015, AJ, 150, 150
Girardi L., Bressan A., Bertelli G., Chiosi C., 2000, A&AS, 141, 371
Hao J. et al., 2009, ApJ, 702, 745
Hao J. et al., 2010, ApJS, 191, 254
Hoeting J. A., Madigan D., Raftery A. E., Volinsky C. T., 1999, Stat. Sci., 14, 382
Hollowood D. L. et al., 2019, ApJS, 244, 22
Hoyle B. et al., 2018, MNRAS, 478, 592
Ivezić Ž. et al., 2008, preprint (arXiv:0805.2366)
Jansen F. A., Laine R., 1997, Bulletin of the American Astronomical Society, Vol. 29, American Astronomical Society Meeting Abstracts. p. 1365
Kaiser N., 1991, ApJ, 383, 104
Kelly B. C., 2007, ApJ, 665, 1489
Kinney A. L., Calzetti D., Bohlin R. C., McQuade K., Storchi-Bergmann T., Schmitt H. R., 1996, ApJ, 467, 38
Koester B. P. et al., 2007, ApJ, 660, 239
Koopmans A. L. H., Owen D. B., Rosenblatt J. I., 1964, Biometrika, 51, 25
Laigle C. et al., 2016, ApJS, 224, 24
Laureijs R. et al., 2011, preprint (arXiv:1110.3193)
Lieu M. et al., 2016, A&A, 592, A4
Lloyd-Davies E. J. et al., 2011, MNRAS, 418, 14
Logan C. H. A. et al., 2018, A&A, 620, A18
Mahajan S., Raychaudhury S., 2009, MNRAS, 400, 687
Mahdavi A., Hoekstra H., Babul A., Bildfell C., Jeltema T., Henry J. P., 2013, ApJ, 767, 116
Mantz A. B., Allen S. W., Morris R. G., Schmidt R. W., von der Linden A., Urban O., 2015, MNRAS, 449, 199
Mantz A. B. et al., 2016, MNRAS, 463, 3582
Marigo P., Girardi L., 2007, A&A, 469, 239
Marigo P., Girardi L., Bressan A., Groenewegen M. A. T., Silva L., Granato G. L., 2008, A&A, 482, 883
Melchior P. et al., 2017, MNRAS,469, 4899
Miller C. J. et al., 2005, AJ, 130, 968
Mitchell P. D., Lacey C. G., Baugh C. M., Cole S., 2013, MNRAS, 435, 87
Mohr J. J. et al., 2012, in Radziwill N. M., Chiozzi G., eds, Proc. SPIE Conf. Ser. Vol. 8451, Software and Cyberinfrastructure for Astronomy II. SPIE, Bellingham, p. 84510D
Mulroy S. L. et al., 2019, MNRAS, 484, 60
Navarro J. F., Frenk C. S., White S. D. M., 1996, ApJ, 462, 563
Oemler A., Jr, 1974, ApJ, 194, 1
Oguri M., 2014, MNRAS, 444, 147
Palmese A. et al., 2016, MNRAS, 463, 1486
Pereira M. E. S. et al., 2018, MNRAS, 474, 1361
Press W. H., Schechter P., 1974, ApJ, 187, 425
Rozo E. et al., 2009a, ApJ, 699, 768
Rozo E. et al., 2009b, ApJ, 703, 601
Rozo E., Rykoff E., Koester B., Nord B., Wu H.-Y., Evrard A., Wechsler R., 2011, ApJ, 740, 53
Rykoff E. S. et al., 2014, ApJ, 785, 104
Rykoff E. S. et al., 2016, ApJS, 224, 1
Sánchez-Blázquez P. et al., 2006, MNRAS, 371, 703
Sevilla I. et al., 2011, preprint (astro-ph/1109.6741)
Sheth R. K., Tormen G., 2002, MNRAS, 329, 61
Simet M., McClintock T., Mandelbaum R., Rozo E., Rykoff E., Sheldon E., Wechsler R. H., 2017, MNRAS, 466, 3103
Simha V., Weinberg D. H., Conroy C., Dave R., Fardal M., Katz N., Oppenheimer B. D., 2014, preprint (arXiv:1404.0402)
Soares-Santos M. et al., 2011, ApJ, 727, 45
Taylor M. B., 2005, in Shopbell P., Britton M., Ebert R., eds, ASP Conf. Ser. Vol. 347, Astronomical Data Analysis Software and Systems XIV. Astron. Soc. Pac., San Francisco, p. 29
Taylor E. N. et al., 2011, MNRAS, 418, 1587
The Dark Energy Survey Collaboration, 2005, preprint (astro-ph/0510346)
Tinker J., Kravtsov A. V., Klypin A., Abazajian K., Warren M., Yepes G., Gottlöber S., Holz D. E., 2008, ApJ, 688, 709
Wechsler R. H., Tinker J. L., 2018, ARA&A, 56, 435
Zhang Y. et al., 2017, preprint (arXiv:1710.05908)
Zu Y., Mandelbaum R., 2016, MNRAS, 457, 4360

APPENDIX A: CLUSTER CATALOGUES

In Tables A1 and A2, we provide the optical and X-ray properties of *Chandra* and *XMM* clusters. z_λ is the cluster photometric redshift computed by redMaPPer. $\mu_\star$ is the mass proxy computed in this work, while the redMaPPer richness is λ. The full redMaPPer DES Y1A1 catalogues will be available at http://risa.stanford.edu/redmapper/. `XCS_NAME` in Table A2 is the unique source identifier which could be used to match with the XCS source catalogue (Giles et al., in preparation).

Table A1. *Chandra* clusters.

z_λ	RA	Dec.	λ	$\mu_\star$	kT_X (keV)	Obsid(s)
0.304	79.156	− 54.500	200.65 ± 6.90	2265.61 ± 193.89	$10.90^{+0.84}_{-0.81}$	9331,15099
0.419	62.796	− 48.328	171.91 ± 4.49	2393.20 ± 181.40	$7.39^{+0.41}_{-0.32}$	13396,16355,17536
0.301	41.353	− 53.029	144.10 ± 4.00	2133.15 ± 192.72	$10.24^{+0.26}_{-0.26}$	12260,16127,16282,16524,16525,16526
0.351	342.216	− 44.518	188.40 ± 10.06	2465.34 ± 212.46	$14.89^{+0.59}_{-0.55}$	4966
0.368	10.208	− 44.131	138.85 ± 4.72	1381.93 ± 148.01	$7.88^{+1.08}_{-0.80}$	13395
0.240	323.810	1.406	136.44 ± 4.69	2207.50 ± 235.86	$12.16^{+1.36}_{-0.92}$	15097
0.326	323.800	− 1.050	142.26 ± 6.28	2066.69 ± 217.81	$9.48^{+0.73}_{-0.53}$	11710,16285
0.526	308.795	− 52.856	159.39 ± 6.29	1906.99 ± 120.57	$7.51^{+3.04}_{-1.41}$	13466
0.278	354.416	0.271	132.86 ± 4.36	1743.45 ± 193.26	$9.46^{+0.66}_{-0.45}$	3248,11728
0.605	89.930	− 52.824	165.92 ± 5.63	1580.90 ± 130.39	$7.71^{+0.84}_{-0.55}$	12264,13116,13117
0.282	319.704	0.560	130.37 ± 4.73	941.93 ± 122.49	$6.25^{+2.57}_{-1.30}$	17162,16271,17162
0.591	356.198	− 42.731	152.04 ± 5.00	2074.08 ± 194.61	$14.32^{+0.52}_{-0.52}$	13401,16135,16545
0.418	69.574	− 54.322	124.99 ± 4.26	1522.08 ± 296.48	$11.83^{+1.25}_{-0.90}$	12259
0.231	305.837	− 55.597	135.36 ± 6.69	1769.49 ± 166.19	$9.88^{+0.79}_{-0.66}$	15108
0.348	10.265	− 44.500	125.67 ± 5.83	1186.05 ± 136.16	$5.86^{+0.63}_{-0.37}$	17185
0.425	323.906	− 57.442	130.46 ± 6.13	1601.02 ± 119.29	$7.00^{+1.13}_{-0.77}$	13463
0.443	46.070	− 44.025	138.20 ± 6.42	1216.62 ± 118.77	$8.67^{+1.20}_{-1.07}$	13402
0.107	52.128	− 55.705	98.49 ± 4.57	1556.41 ± 153.54	$6.90^{+0.33}_{-0.33}$	15313
0.343	34.272	− 52.713	121.80 ± 5.16	1713.03 ± 162.38	$8.93^{+2.15}_{-1.36}$	12269
0.637	20.796	− 48.356	137.04 ± 5.68	1629.48 ± 175.04	$6.26^{+0.86}_{-0.61}$	13491
0.485	328.636	− 0.817	112.56 ± 4.59	1425.71 ± 218.74	$9.81^{+1.63}_{-1.05}$	16230
0.482	326.463	− 56.749	124.29 ± 5.23	1851.69 ± 128.73	$9.02^{+1.65}_{-1.18}$	13398
0.536	53.827	− 40.595	118.49 ± 4.75	1362.55 ± 116.42	$10.25^{+6.73}_{-2.71}$	9416
0.405	46.067	− 49.357	99.65 ± 3.90	1175.95 ± 102.05	$6.79^{+0.61}_{-0.57}$	12265
0.585	64.346	− 47.813	103.10 ± 4.53	1319.48 ± 216.97	$7.03^{+0.60}_{-0.55}$	13397
0.401	38.687	− 58.521	99.89 ± 3.76	1163.74 ± 93.37	$8.33^{+1.09}_{-0.96}$	13403
0.282	38.939	− 51.351	94.42 ± 3.58	1045.47 ± 131.45	$7.58^{+0.79}_{-0.59}$	12262
0.261	355.948	0.257	97.13 ± 5.50	872.69 ± 130.77	$6.29^{+0.28}_{-0.28}$	5786,17170,17490,18702,18703
0.357	57.068	− 45.263	89.86 ± 3.96	1073.72 ± 132.79	$6.18^{+0.98}_{-0.80}$	13465
0.531	56.730	− 54.650	107.99 ± 5.15	791.36 ± 79.59	$4.84^{+0.69}_{-0.53}$	12270,13155
0.337	39.257	− 49.636	82.20 ± 3.45	806.08 ± 131.55	$5.06^{+0.51}_{-0.49}$	12266
0.317	358.791	− 50.941	93.97 ± 4.67	948.72 ± 103.81	$4.70^{+0.50}_{-0.37}$	11998
0.290	38.103	− 44.328	133.10 ± 10.07	1055.20 ± 81.84	$11.31^{+1.35}_{-1.07}$	4993
0.207	77.573	− 45.322	84.93 ± 4.41	826.01 ± 114.00	$7.91^{+0.55}_{-0.50}$	15111
0.222	36.492	− 41.882	101.77 ± 6.80	867.17 ± 111.58	$6.79^{+0.29}_{-0.29}$	15110,17476
0.430	52.737	− 52.470	110.63 ± 6.45	880.08 ± 83.50	$5.60^{+0.82}_{-0.59}$	893
0.428	338.315	− 53.653	93.52 ± 4.60	1261.95 ± 150.78	$6.76^{+0.92}_{-0.81}$	13504
0.115	341.562	− 52.721	81.27 ± 3.48	1271.34 ± 209.00	$10.29^{+0.71}_{-0.71}$	15304
0.188	81.454	− 47.252	72.33 ± 3.17	569.79 ± 70.29	$7.67^{+0.54}_{-0.45}$	15122
0.590	44.088	− 56.303	82.09 ± 3.98	803.66 ± 99.32	$7.11^{+1.11}_{-0.76}$	13481,14448
0.564	38.178	− 52.956	84.61 ± 3.93	1009.03 ± 165.45	$6.14^{+1.91}_{-1.17}$	12263
0.498	30.142	− 48.871	81.69 ± 3.68	1202.31 ± 114.41	$11.56^{+3.81}_{-2.01}$	13487
0.649	85.709	− 41.000	113.97 ± 6.46	1248.34 ± 125.15	$7.82^{+1.17}_{-0.80}$	914
0.301	80.565	− 48.305	90.48 ± 4.76	1746.10 ± 143.65	$4.72^{+0.58}_{-0.37}$	4208
0.645	40.863	− 59.517	90.19 ± 5.08	1108.13 ± 140.96	$8.96^{+1.18}_{-0.85}$	13484,15573

Table A1 *– continued*

z_λ	RA	Dec.	λ	$\mu_\star$	kT_X (keV)	Obsid(s)
0.313	359.138	− 50.953	73.50 ± 3.26	926.14 ± 107.00	$2.14^{+0.48}_{-0.33}$	11746
0.109	78.664	− 49.058	70.02 ± 3.39	1243.21 ± 134.28	$5.45^{+0.36}_{-0.34}$	4980
0.410	3.330	− 49.111	104.42 ± 7.85	724.34 ± 88.97	$7.13^{+0.87}_{-0.67}$	13462
0.246	322.413	0.086	75.56 ± 5.47	912.49 ± 165.76	$7.25^{+0.18}_{-0.18}$	552,9370
0.565	46.961	− 50.701	75.10 ± 4.04	935.19 ± 189.65	$8.16^{+1.06}_{-0.84}$	13476
0.153	72.485	− 44.673	61.86 ± 3.46	526.95 ± 64.93	$4.53^{+0.16}_{-0.16}$	9417,16280
0.629	66.517	− 54.925	73.29 ± 4.06	1189.79 ± 242.52	$8.51^{+3.09}_{-1.67}$	13472
0.568	74.117	− 51.276	88.73 ± 5.90	1095.82 ± 158.79	$8.11^{+1.15}_{-0.86}$	13474
0.471	53.546	− 46.996	69.12 ± 3.47	743.56 ± 88.51	$6.48^{+0.72}_{-0.62}$	13470
0.103	335.945	− 1.647	67.05 ± 4.54	547.98 ± 73.66	$6.14^{+0.23}_{-0.21}$	15107,15312
0.455	77.339	− 53.704	81.02 ± 6.04	751.97 ± 98.22	$9.85^{+1.67}_{-1.13}$	9432
0.114	334.942	− 52.432	64.35 ± 3.38	1121.34 ± 128.50	$4.90^{+0.53}_{-0.44}$	9383
0.657	58.240	− 56.798	65.40 ± 3.67	821.83 ± 157.98	$6.63^{+1.36}_{-0.93}$	13490,15571
0.414	43.208	− 48.416	60.15 ± 3.46	782.76 ± 148.14	$7.77^{+1.22}_{-1.00}$	13494
0.474	33.797	− 52.201	62.76 ± 6.45	465.57 ± 67.00	$5.64^{+1.52}_{-1.05}$	12268
0.310	335.811	− 1.660	34.28 ± 2.80	2848.21 ± 245.38	$7.36^{+6.01}_{-2.14}$	15107,15312
0.227	40.947	− 59.618	30.00 ± 2.66	247.16 ± 82.65	$3.41^{+0.99}_{-0.56}$	13484,15573
0.164	54.067	− 40.629	43.28 ± 4.13	584.58 ± 84.78	$6.30^{+0.30}_{-0.29}$	9416
0.403	58.298	− 47.530	23.65 ± 2.21	154.81 ± 64.28	$1.62^{+0.62}_{-0.27}$	16981

Table A2. *XMM* clusters.

z_λ	RA	Dec.	λ	$\mu_\star$	kT_X (keV)	XCS_NAME
0.429	43.575	− 58.951	234.50 ± 7.52	2965.79 ± 204.70	$7.41^{+7.59}_{-7.24}$	XMMXCS J025417.8−585705.2
0.303	79.153	− 54.522	195.07 ± 6.78	2260.15 ± 192.60	$5.76^{+5.86}_{-5.66}$	XMMXCS J051636.6−543120.8
0.352	342.187	− 44.528	178.84 ± 8.71	2464.07 ± 212.98	$10.28^{+10.44}_{-10.12}$	XMMXCS J224844.9−443141.7
0.421	62.809	− 48.320	174.46 ± 5.07	2392.56 ± 181.57	$5.81^{+6.87}_{-4.98}$	XMMXCS J041114.1−481910.9
0.604	89.932	− 52.827	169.08 ± 5.77	1580.02 ± 130.30	$6.89^{+7.60}_{-6.28}$	XMMXCS J055943.5−524937.5
0.301	41.372	− 53.036	146.24 ± 4.04	2151.24 ± 193.82	$8.31^{+8.64}_{-8.00}$	XMMXCS J024529.3−530210.7
0.326	323.799	− 1.049	141.08 ± 5.96	2063.03 ± 217.59	$6.77^{+7.67}_{-6.04}$	XMMXCS J213511.8−010258.0
0.443	46.066	− 44.031	138.53 ± 6.45	1216.62 ± 118.77	$5.86^{+6.10}_{-5.64}$	XMMXCS J030415.7−440153.0
0.231	305.847	− 55.585	136.78 ± 7.18	1643.18 ± 160.40	$7.93^{+8.50}_{-7.41}$	XMMXCS J202323.2−553504.7
0.239	323.820	1.433	135.48 ± 5.08	2192.19 ± 234.86	$8.51^{+8.78}_{-8.26}$	XMMXCS J213516.8+012600.0
0.425	323.910	− 57.438	130.39 ± 6.17	1682.62 ± 142.32	$6.38^{+7.94}_{-5.25}$	XMMXCS J213538.5−572616.6
0.278	354.411	0.271	129.00 ± 4.30	1740.84 ± 193.03	$7.15^{+7.37}_{-6.94}$	XMMXCS J233738.6+001614.5
0.494	40.914	− 48.561	126.99 ± 4.31	1663.42 ± 173.41	$5.78^{+5.98}_{-5.59}$	XMMXCS J024339.4−483338.3
0.481	326.466	− 56.748	124.41 ± 5.23	1851.19 ± 128.87	$7.18^{+7.77}_{-6.66}$	XMMXCS J214551.9−564453.6
0.346	34.298	− 52.754	119.25 ± 4.42	1727.99 ± 165.14	$4.94^{+5.36}_{-4.58}$	XMMXCS J021711.6−524512.9
0.649	85.710	− 41.001	115.18 ± 6.49	1248.41 ± 125.17	$6.91^{+7.83}_{-6.11}$	XMMXCS J054250.3−410003.5
0.429	52.687	− 52.489	107.32 ± 6.11	878.31 ± 83.43	$4.33^{+4.44}_{-4.23}$	XMMXCS J033044.8−522921.9
0.584	64.345	− 47.813	104.70 ± 4.61	1318.88 ± 216.92	$7.03^{+7.35}_{-6.73}$	XMMXCS J041722.7−474847.1
0.410	3.328	− 49.114	103.78 ± 7.82	723.43 ± 88.67	$6.76^{+8.47}_{-5.60}$	XMMXCS J001318.8−490651.9
0.287	38.073	− 44.348	101.27 ± 6.38	1052.83 ± 81.40	$6.25^{+6.39}_{-6.11}$	XMMXCS J023217.6−442053.8
0.401	38.677	− 58.523	100.89 ± 4.00	1163.61 ± 93.36	$5.53^{+5.73}_{-5.34}$	XMMXCS J023442.5−583121.0
0.106	52.150	− 55.711	98.55 ± 4.63	1548.93 ± 152.71	$4.83^{+4.92}_{-4.74}$	XMMXCS J032835.9−554239.3
0.262	355.924	0.309	93.40 ± 6.24	881.17 ± 131.71	$5.45^{+5.65}_{-5.27}$	XMMXCS J234341.7+001831.2
0.523	354.032	− 53.876	92.45 ± 4.25	1451.25 ± 163.74	$2.97^{+3.75}_{-2.38}$	XMMXCS J233607.6−535232.4
0.300	80.566	− 48.305	91.43 ± 4.92	1745.27 ± 143.40	$3.95^{+4.17}_{-3.75}$	XMMXCS J052215.8−481817.2
0.222	36.473	− 41.913	91.20 ± 4.36	865.47 ± 111.05	$5.07^{+5.19}_{-4.96}$	XMMXCS J022553.4−415448.4
0.207	77.570	− 45.321	86.58 ± 4.46	825.73 ± 113.98	$6.08^{+6.23}_{-5.93}$	XMMXCS J051016.7−451917.2
0.383	18.680	− 41.398	86.38 ± 4.27	1775.89 ± 260.44	$6.21^{+6.56}_{-5.89}$	XMMXCS J011443.1−412351.5

Table A2 – *continued*

z_λ	RA	Dec.	λ	$\mu_\star$	kT_X (keV)	XCS_NAME
0.654	38.258	− 58.325	85.16 ± 5.11	930.11 ± 141.68	$5.29^{+5.60}_{-5.00}$	XMMXCS J023301.8−581928.5
0.409	40.159	− 59.768	83.43 ± 4.16	767.95 ± 135.16	$6.94^{+7.45}_{-6.47}$	XMMXCS J024038.2−594605.3
0.114	341.592	− 52.740	82.41 ± 3.37	1147.89 ± 195.46	$5.24^{+5.30}_{-5.18}$	XMMXCS J224622.0−524422.6
0.540	355.482	− 53.145	80.43 ± 7.59	410.21 ± 49.21	$3.96^{+4.81}_{-3.37}$	XMMXCS J234155.7−530843.5
0.124	26.247	− 53.020	78.69 ± 2.83	1120.11 ± 112.26	$6.28^{+6.36}_{-6.20}$	XMMXCS J014459.1−530113.7
0.101	326.591	− 57.289	78.00 ± 4.23	1591.22 ± 133.73	$3.88^{+3.94}_{-3.81}$	XMMXCS J214621.8−571719.3
0.463	60.968	− 57.328	75.01 ± 4.03	1135.02 ± 142.06	$4.33^{+4.51}_{-4.17}$	XMMXCS J040352.4−571939.7
0.189	81.454	− 47.252	72.82 ± 3.19	567.63 ± 70.24	$6.67^{+6.96}_{-6.39}$	XMMXCS J052548.9−471507.3
0.246	322.416	0.088	71.23 ± 4.94	913.29 ± 165.84	$5.29^{+5.34}_{-5.24}$	XMMXCS J212939.7+000516.9
0.407	58.563	− 59.089	70.42 ± 3.09	982.90 ± 136.59	$4.84^{+5.21}_{-4.52}$	XMMXCS J035415.2−590519.1
0.168	351.553	− 53.316	66.85 ± 4.18	581.55 ± 90.59	$2.81^{+3.52}_{-2.29}$	XMMXCS J232612.8−531858.4
0.102	335.971	− 1.621	66.39 ± 4.43	529.56 ± 71.17	$4.57^{+4.62}_{-4.53}$	XMMXCS J222353.0−013714.4
0.274	349.804	− 54.083	61.95 ± 2.66	399.35 ± 46.23	$2.87^{+3.30}_{-2.53}$	XMMXCS J231912.9−540457.7
0.396	307.707	− 56.633	59.90 ± 3.48	495.71 ± 73.44	$4.18^{+4.46}_{-3.92}$	XMMXCS J203049.5−563758.6
0.547	55.757	− 55.310	59.51 ± 3.67	609.89 ± 121.03	$6.73^{+7.59}_{-5.99}$	XMMXCS J034301.6−551835.5
0.153	72.486	− 44.671	59.12 ± 3.41	527.02 ± 64.94	$3.75^{+3.85}_{-3.65}$	XMMXCS J044956.6−444017.3
0.140	313.985	− 54.930	57.74 ± 2.84	1022.11 ± 175.99	$3.87^{+4.00}_{-3.75}$	XMMXCS J205556.3−545548.2
0.614	349.097	− 59.076	56.95 ± 3.80	693.10 ± 125.43	$2.37^{+3.00}_{-1.95}$	XMMXCS J231623.3−590432.4
0.462	49.316	− 59.590	55.59 ± 4.32	856.54 ± 124.87	$5.32^{+5.65}_{-5.01}$	XMMXCS J031715.7−593525.4
0.599	37.777	− 54.064	52.66 ± 3.22	517.48 ± 88.22	$5.17^{+5.86}_{-4.61}$	XMMXCS J023106.3−540349.9
0.246	322.517	− 0.352	51.44 ± 2.82	885.71 ± 126.48	$2.66^{+2.94}_{-2.43}$	XMMXCS J213004.1−002105.9
0.386	349.335	− 53.960	49.95 ± 2.83	674.86 ± 109.34	$4.16^{+4.82}_{-3.63}$	XMMXCS J231720.4−535734.5
0.460	341.458	− 52.910	48.90 ± 3.47	436.30 ± 53.15	$4.56^{+6.20}_{-3.53}$	XMMXCS J224549.8−525436.4
0.131	307.990	− 56.408	48.53 ± 3.20	385.03 ± 54.84	$4.45^{+4.56}_{-4.34}$	XMMXCS J203157.5−562430.2
0.564	65.610	− 51.674	47.36 ± 3.49	577.55 ± 72.13	$2.81^{+3.04}_{-2.61}$	XMMXCS J042226.4−514025.8
0.393	8.617	− 43.315	46.96 ± 3.27	666.66 ± 129.33	$3.15^{+3.30}_{-3.00}$	XMMXCS J003428.0−431854.2
0.106	25.128	− 54.522	42.60 ± 2.71	895.62 ± 97.66	$3.47^{+3.57}_{-3.36}$	XMMXCS J014030.7−543120.6
0.106	7.567	− 53.420	42.11 ± 3.61	644.67 ± 73.43	$3.06^{+3.15}_{-2.98}$	XMMXCS J003016.0−532513.6
0.428	44.337	− 57.547	41.86 ± 3.04	615.71 ± 85.38	$5.02^{+5.82}_{-4.35}$	XMMXCS J025720.9−573248.9
0.389	351.429	− 53.277	39.18 ± 2.70	573.12 ± 87.95	$1.92^{+2.55}_{-1.55}$	XMMXCS J232543.0−531635.8
0.422	15.126	− 47.822	39.12 ± 2.87	554.71 ± 95.61	$2.56^{+2.78}_{-2.36}$	XMMXCS J010030.2−474919.6
0.584	56.091	− 53.678	38.90 ± 3.91	316.50 ± 69.14	$1.78^{+2.23}_{-1.49}$	XMMXCS J034421.9−534042.5
0.564	353.376	− 52.253	38.75 ± 3.13	723.56 ± 108.57	$2.12^{+2.85}_{-1.69}$	XMMXCS J233330.2−521511.5
0.218	8.443	− 43.292	38.46 ± 2.44	348.25 ± 76.23	$2.32^{+2.43}_{-2.21}$	XMMXCS J003346.3−431729.7
0.562	38.041	− 57.766	37.59 ± 3.18	216.50 ± 59.47	$3.32^{+3.88}_{-2.88}$	XMMXCS J023209.8−574558.9
0.373	64.187	− 55.419	37.20 ± 2.91	399.58 ± 63.64	$2.29^{+2.90}_{-1.89}$	XMMXCS J041644.8−552506.6
0.410	36.868	− 40.850	36.69 ± 2.72	374.30 ± 93.59	$4.40^{+5.26}_{-3.73}$	XMMXCS J022728.2−405101.7
0.416	19.957	− 44.076	35.96 ± 2.87	459.85 ± 86.98	$2.67^{+3.35}_{-2.21}$	XMMXCS J011949.7−440434.5
0.136	322.613	− 0.008	35.11 ± 2.50	341.51 ± 49.72	$2.51^{+2.86}_{-2.23}$	XMMXCS J213027.0−000029.7
0.310	335.811	− 1.660	34.66 ± 2.84	2850.61 ± 245.68	$3.85^{+4.15}_{-3.58}$	XMMXCS J222314.6−013936.8
0.422	85.468	− 40.877	33.60 ± 2.92	360.23 ± 96.59	$4.36^{+5.25}_{-3.69}$	XMMXCS J054152.3−405236.4
0.318	354.186	− 53.802	32.10 ± 2.58	430.69 ± 107.72	$2.31^{+3.00}_{-1.89}$	XMMXCS J233644.6−534806.9

[1]*Fermi National Accelerator Laboratory, PO Box 500, Batavia, IL 60510, USA*
[2]*Department of Physics & Astronomy, University College London, Gower Street, London WC1E 6BT, UK*
[3]*Department of Astronomy, The Ohio State University, Columbus, OH 43210, USA*
[4]*Department of Physics, Carnegie Mellon University, Pittsburgh, PA 15312, USA*
[5]*Physics Department, Brandeis University, 415 South Street, Waltham, MA 02453, USA*
[6]*Kavli Institute for Cosmological Physics, University of Chicago, Chicago, IL 60637, USA*
[7]*Department of Physics and Astronomy, Pevensey Building, University of Sussex, Brighton BN1 9QH, UK*
[8]*Santa Cruz Institute for Particle Physics, Santa Cruz, CA 95064, USA*
[9]*Department of Astronomy, University of Michigan, Ann Arbor, MI 48109, USA*
[10]*Department of Physics, University of Michigan, Ann Arbor, MI 48109, USA*

[11]*Astrophysics & Cosmology Research Unit, School of Mathematics, Statistics & Computer Science, University of KwaZulu-Natal, Westville Campus, Durban 4041, South Africa*
[12]*Department of Physics, Stanford University, 382 Via Pueblo Mall, Stanford, CA 94305, USA*
[13]*Kavli Institute for Particle Astrophysics & Cosmology, Stanford University, PO Box 2450, Stanford, CA 94305, USA*
[14]*SLAC National Accelerator Laboratory, Menlo Park, CA 94025, USA*
[15]*Department of Physics, ETH Zurich, Wolfgang-Pauli-Strasse 16, CH-8093 Zurich, Switzerland*
[16]*CCPP, New York University, New York, NY 10003, USA*
[17]*Department of Physics, University of Arizona, Tucson, AZ 85721, USA*
[18]*Max Planck Institute for Extraterrestrial Physics, Giessenbachstrasse, D-85748 Garching, Germany*
[19]*Fakultät für Physik, Universitäts-Sternwarte, Ludwig-Maximilians Universität München, Scheinerstr 1, D-81679 München, Germany*
[20]*Institute of Cosmology and Gravitation, University of Portsmouth, Portsmouth PO1 3FX, UK*
[21]*Centro de Investigaciones Energéticas, Medioambientales y Tecnológicas (CIEMAT), E-28040 Madrid, Spain*
[22]*Laboratório Interinstitucional de e-Astronomia - LIneA, Rua Gal. José Cristino 77, Rio de Janeiro, RJ - 20921-400, Brazil*
[23]*Department of Astronomy, University of Illinois at Urbana-Champaign, 1002 W. Green Street, Urbana, IL 61801, USA*
[24]*National Center for Supercomputing Applications, 1205 West Clark St., Urbana, IL 61801, USA*
[25]*Institut de Física d'Altes Energies (IFAE), The Barcelona Institute of Science and Technology, Campus UAB, E-08193 Bellaterra (Barcelona), Spain*
[26]*Institut d'Estudis Espacials de Catalunya (IEEC), E-08034 Barcelona, Spain*
[27]*Institute of Space Sciences (ICE, CSIC), Campus UAB, Carrer de Can Magrans s/n, E-08193 Barcelona, Spain*
[28]*Astrophysics Research Institute, Liverpool John Moores University, IC2, Liverpool Science Park, 146 Brownlow Hill, Liverpool L3 5RF, UK*
[29]*Observatório Nacional, Rua Gal. José Cristino 77, Rio de Janeiro, RJ - 20921-400, Brazil*
[30]*Department of Physics, IIT Hyderabad, Kandi, Telangana 502285, India*
[31]*Excellence Cluster Origins, Boltzmannstr 2, D-85748 Garching, Germany*
[32]*Faculty of Physics, Ludwig-Maximilians-Universität, Scheinerstr 1, D-81679 Munich, Germany*
[33]*Instituto de Fisica Teorica UAM/CSIC, Universidad Autonoma de Madrid, E-28049 Madrid, Spain*
[34]*Center for Cosmology and Astro-Particle Physics, The Ohio State University, Columbus, OH 43210, USA*
[35]*Department of Physics, The Ohio State University, Columbus, OH 43210, USA*
[36]*Harvard–Smithsonian Center for Astrophysics, Cambridge, MA 02138, USA*
[37]*Department of Astronomy/Steward Observatory, University of Arizona, 933 North Cherry Avenue, Tucson, AZ 85721-0065, USA*
[38]*Australian Astronomical Optics, Macquarie University, North Ryde, NSW 2113, Australia*
[39]*Institute for Astronomy, University of Edinburgh, Royal Observatory, Blackford Hill, Edinburgh EH9 3HJ, UK*
[40]*Departamento de Física Matemática, Instituto de Física, Universidade de São Paulo, CP 66318, São Paulo, SP 05314-970, Brazil*
[41]*Institute for Astronomy, University of Edinburgh, Royal Observatory, Blackford Hill, Edinburgh EH9 3NJ, UK*
[42]*George P. and Cynthia Woods Mitchell Institute for Fundamental Physics and Astronomy, Texas A&M University, College Station, TX 77843, USA*
[43]*Department of Physics and Astronomy, Texas A&M University, College Station, TX 77843, USA*
[44]*Institució Catalana de Recerca i Estudis Avançats, E-08010 Barcelona, Spain*
[45]*Department of Astrophysical Sciences, Princeton University, Peyton Hall, Princeton, NJ 08544, USA*
[46]*BIPAC, Department of Physics, University of Oxford, Denys Wilkinson Building, 1 Keble Road, Oxford OX1 3RH, UK*
[47]*Instituto de Física Gleb Wataghin, Universidade Estadual de Campinas, Campinas, SP 13083-859, Brazil*
[48]*Sub-department of Astrophysics, Department of Physics, University of Oxford, Denys Wilkinson Building, Keble Road, Oxford OX1 3RH, UK*
[49]*Department of Physics, Lancaster University, Lancaster LA1 4 YB, UK*
[50]*Computer Science and Mathematics Division, Oak Ridge National Laboratory, Oak Ridge, TN 37831, USA*
[51]*Departamento de Física e Astronomia, Faculdade de Ciencias, Universidade do Porto, Rua do Campo Alegre, 687, P-4169-007 Porto, Portugal*
[52]*Instituto de Astrofísica e Ciencias do Espaco, Universidade do Porto, CAUP, Rua das Estrelas, P-4150-762 Porto, Portugal*
[53]*Argonne National Laboratory, 9700 South Cass Avenue, Lemont, IL 60439, USA*
[54]*Cerro Tololo Inter-American Observatory, National Optical Astronomy Observatory, Casilla 603, La Serena, Chile*

This paper has been typeset from a TEX/LATEX file prepared by the author.